The endosomal sorting complex Retromer has a central role in systemic cholesterol homeostasis by controlling endo-lysosomal cholesterol transport in hepatocytes

Dyonne Y. Vos[1], Markus G. Barbosa[1], Andries H. Heida[1], W. Alfredo Ríos-Ocampo[1], Joël J. Tissink[1,2], Mirjam H. Koster[1], Marieke Smit[1], Nicolette Huijkman[1], Niels J. Kloosterhuis[1], Rick Havinga[1,3], Marceline M. Fuh[4], Johan W. Jonker[1], Fulvio Reggiori[5,6], Muriel Mari[5], Ludger Scheja[4], Joerg Heeren[4], Folkert Kuipers[1,7], Jan Freark de Boer[1,3], Justina C. Wolters[1], Jan Albert Kuivenhoven[1], Bart van de Sluis[1]

[1] Department of Pediatrics, [3] Department of Laboratory Medicine, and [7] European Research Institute for the Biology of Ageing (ERIBA), University of Groningen, University Medical Center Groningen, Groningen, the Netherlands; [2] Institute for Diabetes and Cancer, Helmholtz Center Munich, Neuherberg, Germany; [4] Department of Biochemistry and Molecular Cell Biology, University Medical Center Hamburg-Eppendorf, Hamburg, Germany; [5] Department of Biomedicine, Aarhus University, Aarhus, Denmark; [6] Aarhus Institute for Advanced Studies (AIAS), Aarhus University, Aarhus, Denmark

Abstract

Disturbed cholesterol homeostasis is associated with multiple diseases, such as atherosclerotic cardiovascular disease, lysosomal storage disorders, and neurodegenerative disorders. The endo-lysosomal network plays a central role in the distribution of cholesterol between subcellular membranes, but the processes controlling this transport are still not well-defined. Here, we investigate the impact of hepatic Retromer, an endosomal sorting complex consisting of VPS35, VPS26, and VPS29, on cholesterol homeostasis by using a liver-specific VPS35-deficient (*Vps35*^{HepKO}) mouse model. Hepatic VPS35 deficiency strongly reduces the function of the lysosomal proteins lysosomal acid lipase (LAL), scavenger receptor class B member 2 (SCARB2), and Niemann-Pick type C1 (NPC1), concomitant with hepatic cholesterol accumulation in lysosomal compartments, delayed transport of endocytosed cholesterol through the endo-lysosomal network, and increased cholesterol biosynthesis. In addition, the levels and intracellular distribution of low-density lipoprotein receptor (LDLR) and LDLR-related protein 1 (LRP1) are affected, likely explaining increased plasma LDL-cholesterol in *Vps35*^{HepKO} mice. High-fat/high-cholesterol diet feeding exacerbates hepatic and plasma cholesterol content in *Vps35*^{HepKO} mice and leads to mild liver injury, hepatic inflammation, and increased hepatocellular proliferation. Altogether, we here uncover that, in addition to its established function in the endosomal sorting of integral membrane proteins, Retromer plays a key role in lysosomal cholesterol egress.

Introduction

Cholesterol is essential for membrane integrity in all mammalian cells and is a precursor of bile acids, steroid hormones, and vitamin D. An imbalance in cholesterol homeostasis is associated with various disorders, including atherosclerotic cardiovascular disease (ASCVD), lysosomal storage disorders, such as Niemann-Pick type C (NPC) disease and lysosomal acid lipase deficiency (LAL-D), and neurodegenerative disorders, such as Alzheimer's and Parkinson's disease (1–3).

Cellular cholesterol homeostasis requires strict regulation of *de novo* cholesterol synthesis and cholesterol uptake. Cellular uptake of cholesterol relies on receptor-mediated endocytosis of cholesterol-rich lipoproteins, such as low-density lipoprotein (LDL) (4). After internalization and transport through the endo-lysosomal network, the lipoprotein-derived cholesteryl esters (CE) are hydrolyzed in lysosomes by lysosomal acid lipase (LAL) to release fatty acids (FA) and free cholesterol (FC) (5). Lysosomal FC egress is controlled by NPC proteins. The small luminal NPC2 protein binds FC and delivers it to the lysosomal membrane transporter NPC1 (6). Together they enable the distribution of FC to the plasma membrane (PM), endoplasmic reticulum (ER), and trans-Golgi network (TGN) (7). It has recently been shown that the scavenger receptor class B member 2 (SCARB2), also known as lysosomal integral membrane protein type 2 (LIMP2), acts in parallel with NPCs to mediate lysosomal cholesterol export (8). In the ER, where FC levels are very low under normal conditions (9), cholesterol is sensed by the sterol regulatory-element binding protein (SREBP)/SREBP cleavage-activating protein (SCAP) machinery to regulate cholesterol biosynthesis and LDL-cholesterol uptake accordingly (10).

The importance of the endo-lysosomal system in cellular cholesterol homeostasis is demonstrated by patients with LAL-D (MIM #613497) or NPC disease (MIM #257220, MIM #607625), which are rare disorders caused by loss-of-function mutations in *LIPA*, the gene encoding for LAL, or in the genes encoding the NPC proteins, respectively (11, 12). LAL-D is characterized by the accumulation of CE in late endosomes and lysosomes, which mainly

affects macrophages, spleen, and liver (MIM #613497). Complete loss of LAL in humans results in early-onset Wolman's disease, which is fatal within the first year of life (MIM #620151) (11). Milder mutations in LAL cause cholesteryl ester storage disease (CESD; MIM #278000), which has a later onset due to 5-10% residual LAL activity, resulting in a range of clinical phenotypes, including dyslipidemia, premature atherosclerosis, hepatosplenomegaly, and progressive liver disease (11, 13). NPC disease (MIM #257220, MIM #607625), characterized by FC accumulation in lysosomes of different organs, is primarily a neurodegenerative disorder (12). However, it also leads to progressive liver disease associated with hepatosplenomegaly, cholestasis, and fibrosis (12, 14). To date, no cures are available for LAL-D nor NPC disease and current treatments only alleviate symptoms (12, 13). Despite the well-described roles of LAL and the NPC proteins in lysosomes in controlling cellular cholesterol homeostasis, the mechanisms regulating their levels and functions are ill-defined.

Recent studies have implied a role for the trimeric protein complex Retromer in cholesterol homeostasis. Retromer consists of the vacuolar protein sorting (VPS)26, VPS29, and VPS35, and is mainly localized to endosomal membranes. In concert with sorting nexins (SNXs), like SNX27, Retromer regulates the endosomal sorting of an array of integral membrane proteins ('cargos') and recycles these to the plasma membrane or to the TGN for reuse (15–18). Marquer *et al.* were the first to link Retromer dysfunction to aberrant cholesterol homeostasis (19). They showed that transport of NPC2 from the TGN to the lysosome is mediated via the cation-independent (CI) mannose-6-phosphate receptor (M6PR) (19). CI-M6PR is a Retromer-dependent cargo (20, 21) and loss of Retromer causes lysosomal cholesterol accumulation in HeLa cells due to impaired CI-M6PR retrograde trafficking (19). Others showed that cholesterol accumulation in NPC1-deficient models is associated with reduced Retromer function (22). Furthermore, it is well-established that Retromer interacts with other endosomal sorting complexes, such as the Wiskott-Aldrich syndrome protein and SCAR homolog (WASH) and the COMMD/CCDC22/CCDC93 (CCC) complexes (23). These two complexes act together to facilitate the endosomal recycling of the LDL receptor (LDLR) and

its family member LDLR-related protein 1 (LRP1), which are key for hepatic cholesterol uptake (24–26).

Together, these data strongly suggest a role for Retromer in controlling cholesterol homeostasis, but the molecular connection and physiological relevance remain to be fully elucidated. To this end, we genetically ablated the Retromer subunit *Vps35* in mouse livers, the key organ in regulating systemic cholesterol homeostasis in mammals and find that Retromer has a central role in lysosomal cholesterol egress and hepatic cholesterol uptake.

Materials and Methods

Animals

Mice carrying a *Vps35* allele flanked with *LoxP* sites (*Vps35*$^{fl/fl}$; 129/Ola background) (27) were crossed with a transgenic mouse line (C57Bl/6 background) expressing Cre recombinase under the control of the *Albumin* (*Alb*) gene promoter (#003574, The Jackson Laboratory), to generate a liver-specific *Vps35* knockout (*Vps35*^{HepKO}) mouse model.

All animal experiments were approved by The Central Authority for Scientific Procedures on Animals (CCD), as well as by the Animal Welfare Body (IvD) of the University of Groningen (Groningen, the Netherlands). Male mice were used for the experiments, except for primary hepatocyte experiments, in which both male and female mice were used. Mice were individually housed under a 12-hour light-dark cycle and were fed *ad libitum* with standard laboratory diet (V1554-703, Ssniff Spezialdiäten GmbH), or cholesterol-enriched high-fat (HFC) diet (60% fat, 0.25% cholesterol; D14010701, Research Diets), and water. Body composition (lean, fat, and fluid mass) was measured after 12 weeks of HFC diet-feeding in unanesthetized mice, using nuclear magnetic resonance (NMR) MiniSpec (MiniSpec LF90 BCA-analyzer, Bruker).

Mice were sacrificed after 4 hours of fasting. Blood was collected through cardiac puncture under anesthesia in EDTA-coated tubes. Plasma was collected after centrifugation at 1000 x *g* for 10 min at 4°C. Liver tissues were harvested and either snap-frozen in liquid nitrogen and stored at -80°C until further analysis, or fixed in 4% paraformaldehyde, embedded in paraffin, and cut into 4 µm sections for histological analysis.

VLDL-TG production assay

After 4 hours of fasting, mice were injected intraperitoneally with Poloxamer-407 (Sigma) solution in PBS (1 g per kg body weight) to block lipoprotein lipase (LPL) activity. Blood samples were taken from the tail vein at time points 0, 30, 60, 120, and 240 minutes after Poloxamer-407 injection. Blood samples were centrifuged at 1000 x *g* for 10 min at 4°C to

collect plasma, which was used for triglyceride measurements. In addition, nascent VLDL particles (d<1.006 g/ml) were isolated from plasma collected at t=240min by density gradient ultracentrifugation. Gradients were centrifuged overnight at 40000 rpm in a Beckman Coulter SW41 Ti rotor at 4°C. Concentrations of triglycerides, cholesterol, and phospholipids were measured, and ApoB levels were determined with targeted proteomics.

Cholesterol flux measurements

Cholesterol fluxes were measured using a dual stable isotope tracer method as previously described (28). To determine intestinal cholesterol absorption, mice were administered cholesterol-D_5 and cholesterol-D_7, as follows: 0.3 mg cholesterol-D_5 (Medical Isotopes Inc., Pelham, NH) was dissolved in 150 µL 20% Intralipid (Fresenius Kabi, Den Bosch, the Netherlands) and was injected intravenously. 0.6 mg cholesterol-D_7 (Cambridge Isotope Laboratories, Inc., Andover, MA) was dissolved in 200 µL medium-chain triglyceride oil and was administered by oral gavage. Bloodspots were collected from the tail vein prior to and at 3, 6, 9, 12, 24, 36, 48, 60, 72, 96, 120, 144, and 168 hours after administration for measurement of tracer enrichments. Standard pharmacokinetics were applied for fitting the enrichment curves using SAAM-II software (version 2.3, The Epsilon Group, Charlottesville, VA). The formula used for curve fitting was $f(t) = f_1 e^{-k1t} + f_2 e^{-k2t} - f_3 e^{-k3t}$.

To assess whole-body cholesterol synthesis using mass isotopomer distribution analysis (MIDA) (29, 30), mice received drinking water containing 2% [1-^{13}C] acetate and bloodspots were collected at 0, 24, 33, 48, 57, 72, 81, 96, 105, and 120 hours. After the final time point, mice were sacrificed, and livers were collected for biochemical characterization.

Histological analysis

Paraffin-embedded liver samples were cut into sections of 4 µm, which were stained with hematoxylin-eosin (H&E) and Sirius Red, and for F4/80, Ki67, Bromodeoxyuridine (BrdU), CD11b, B220, CD3, and cytokeratin 19 (CK19); antibodies are listed in Supplemental Table 1. Cell death was assessed by Terminal deoxynucleotidyl transferase-mediated dUTP nick-end

labeling (TUNEL; S7100, Merck Millipore). Images were obtained with a Leica DM3000 microscope with a mounted Leica DFC420 camera. To quantify the TUNEL, Ki67, and BrdU-positive cells, the number of positive cells was counted in ten high-power fields with 20x magnification for each liver sample of each experimental group. For each sample, the average of positive cells per field was calculated, which was used to calculate the average per field per experimental group.

Scanning transmission electron microscopy

For EM analysis, small pieces of fresh liver (1-2 mm^3) were fixed in 2% paraformaldehyde and 2% glutaraldehyde in 0.1 M sodium cacodylate buffer (pH 7.4) at 4°C. Further tissue processing, including staining with neodymium, sectioning, and image acquisition was performed as previously described (31, 32). The files are available upon request.

Hepatic lipid extraction

Liver homogenates (15% w/v in PBS) were used for lipid extraction according to Bligh and Dyer (33). 200 µl of liver homogenate was added to 600 µl of demi-water, mixed with 3 ml chloroform/methanol (1:2 v/v) in a glass tube, and incubated for 30 minutes. Then, 1.2 ml of H_2O and 1 ml of chloroform were added, mixed, and samples were centrifuged at 500 x *g* for 10 minutes at room temperature. The organic layer was transferred to a new glass tube, and the solvent was evaporated with nitrogen at 50°C. The dried lipids were dissolved in 1 ml chloroform, from which 400 µl was again dried and dissolved in 500 µl Triton X-100 2% in chloroform, and evaporated with nitrogen at 50°C. Then, 500 µl demi-water was added, and samples were incubated for 15 minutes at 37°C before further analysis for cholesterol and triglyceride concentrations.

Lipid measurements in plasma, isolated VLDL, and liver

Colorimetric assays were used to determine total cholesterol, free cholesterol, triglyceride, and phospholipid concentrations. Cholesterol enzymatic reagents were used to determine total

cholesterol (#11489232, Roche; Cholesterol FS, DiaSys) and free cholesterol concentrations (#113609910930, DiaSys), with the cholesterol standard FS (DiaSys) as a reference. Triglyceride levels were determined with the Trig/GB kit (#1187771, Roche) or Triglycerides FS (DiaSys), using the Precimat Glycerol standard (Roche) as a reference. Concentrations of phospholipids were determined with the Phospholipid FS kit (DiaSys) and the Phospholipids Standard FS (DiaSys) as a reference.

Lipidomic analysis of liver samples was performed using the Lipidyzer™ Platform (SCIEX, Framingham, MA, USA), as previously described (34).

Fast-performance liquid chromatography (FPLC)

Total cholesterol and triglyceride content of the major lipoprotein classes (VLDL, LDL, and HDL) was determined using FPLC analysis as previously described (35). Briefly, measurements were performed with a system containing a PU-4180 RHPLC pump and a UV-4075 UV-Vis detector (Jasco). Measurements were done in individual plasma samples when enough sample was available, or in pooled plasma samples. The samples, diluted in PBS, were loaded onto a Superose™ 6 Increase 10/300 GL column (GE Healthcare) for separation of lipoproteins at a flow rate of 0.31 ml/min. An enzymatic reagent for cholesterol (Roche) was added through a second flow at a flow rate of 0.1 ml/min.

Liver enzyme measurements in plasma

Concentrations of alanine aminotransferase (ALT) and aspartate aminotransferase (AST) in plasma were measured with a clinical chemistry analyzer (Cobas 6000, Roche Diagnostics), using standard reagents (Roche Diagnostics).

Sucrose gradients

A 20% w/v homogenate was prepared with a piece of snap-frozen liver tissue in homogenization buffer (50 mM Tris-HCl [pH 7.4], 250 mM sucrose, 25 mM KCl, 5 mM $MgCl_2$, 3mM imidazole, supplemented with protease inhibitors [Roche]). To remove nuclei and debris,

homogenates were centrifuged at 1000x*g* for 10 minutes at 4°C. Protein concentrations were determined using the Bradford method (Bio-Rad). 1.5 mg of liver homogenates were loaded onto a 3.7 ml continuous 10% to 40% sucrose gradient, which was centrifuged for 16 hours at 40.000 rpm in a Beckman Coulter SW55 Ti rotor. 370 µl fractions were collected from the top and were used for cholesterol measurements using the Amplex™ Red Cholesterol Assay Kit according to the manufacturer's instructions (A12216, Thermofisher). For further analysis with untargeted proteomics, 30 µl of each fraction was mixed with 10 µl 4× LDS sample buffer.

Cell culture

VPS35-deficient cells were generated in a Cas9-expressing Hepa1-6 murine hepatoma cell line (kindly provided by Noam Zelcer (36)), as previously described (35). Adenovirus to express sgRNAs to target *Vps35* was generated as previously reported (25); sgRNA sequences are listed in Supplemental Table 2. The cells were cultured in Dulbecco's modified Eagle medium (DMEM) GlutaMAX (Gibco), supplemented with 10% fetal calf serum (FCS), 1% penicillin-streptomycin (p/s), and 1.25 µg/ml puromycin, at 37°C and 5% CO2. Subsequently, cells were used for assessment of autophagic flux (described below) and LAL activity (further described below).

To quantitatively measure autophagic flux, Hepa1-6 cells were transduced by retrovirus created with pMRX-IP-GFP-LC3-RFP-LC3ΔG; this plasmid was a gift from Noboru Mizushima (Addgene plasmid #84572, http://n2t.net/addgene:84572; RRID:Addgene_84572) (37). See Supplemental Methods for detailed descriptions of retroviral production and generation of a stable clone. One stable clone was used to transduce three different shRNA sequences (shAtg7, shVps35#1, shVps35#2; see Supplemental Table 2), cloned into pLKO-TRC, or an empty vector as control (EV-control). The pLKO-TRC plasmid was a gift from David Root (Addgene plasmid #10879, http://n2t.net/addgene:10879; RRID:Addgene_10879) (38). After 48 hours of lentiviral incubation, cells were recovered for 16 hours in normal growth medium (DMEM GlutaMAX, 10%FCS, 1% p/s). Before measuring autophagic flux, cells were kept under different conditions: no starvation (normal growth medium), serum starvation (HBSS,

1% FCS, 4,5 g/L D-glucose, 1% p/s), with or without 100nM Bafilomycin A1 treatment (see figure legends for details). Cells were harvested using Accutase (A9664-500ML, Sigma) and were kept on ice in FACS buffer containing 1X HBSS, 2%FCS, 2%BSA. Cells were analyzed with the BD LSR-II cytometer (BD, Biosciences) equipped with a 488-nm laser and 561-nm laser. Data was acquired using DIVA 8.0 software and at least 10.000 events for each sample were acquired. Data was saved as FCS 3.0 or 3.1 files and compensation was not required in any case. Data was processed with Kaluza software (Beckman Coulter). For calculating the autophagic activity, the GFP and RFP mean fluorescence intensity (MFI) (Geometric mean) was used to calculate the GFP/RFP ratio which reversely correlates with autophagic activity.

Primary murine hepatocytes were isolated as described previously (35, 39). These cells were used for biotinylation assays, and for studying NPC1 and SCARB2 levels under different conditions.

Gene expression analysis

A piece of snap-frozen liver tissue was homogenized in QIAzol Lysis Reagent (Qiagen). RNA was isolated by chloroform extraction, precipitated with isopropanol, washed with ethanol, and dissolved in RNase/DNase-free water. 2 µg of RNA were used as input for cDNA synthesis, and 20 ng of cDNA was used for quantitative reverse transcription PCR with the FastStart SYBR Green Master (Roche) and the QuantStudio 7 Flex Real-Time PCR System (Applied Biosystems). The qRT-PCR program was as follows: 50°C/2 minutes; 95°C/10 minutes; 40 cycles with 95°C/15 sec; and 60°C/1 minute. Gene expression was calculated using the ΔΔCT method using QuantStudio Real-Time PCR Software (Applied Biosystems), with *Ppia* expression as an internal control. Primer sets used for gene expression analysis are listed in Supplemental Table 3.

For RNA sequencing analysis, 6 representative liver samples were selected, and total RNA was isolated with the RNAeasy plus kit (#74134, Qiagen) according to the manufacturer's instructions. Quantity and quality were determined using nanodrop and gel electrophoresis, respectively. Library preparation, sequencing, and analysis were done by Novogene Co. Ltd.

Europe. A heatmap was constructed using the z-score calculated from the FPKM values, to visualize the expression of genes involved in cholesterol biosynthesis.

Immunoblotting

Liver and cell samples were homogenized in NP-40 buffer (0.1% Nonidet P-40 [NP-40], 0.4 M NaCl, 10 mM Tris-HCl [pH 8.0], and 1 mM EDTA) supplemented with 1 mM DTT and protease and phosphatase inhibitors (Roche). Protein concentrations were measured with the Bradford assay (Bio-Rad), and samples were diluted in 4x sample buffer. Samples were boiled for 5 minutes at 95°C prior to loading on gel, except for samples used to visualize NPC1 and SCARB2. Proteins were separated with SDS-PAGE and subsequently transferred to Amersham Hybond-P PVDF Transfer Membrane (RPN303F, GE Healthcare). Membranes were blocked in 5% milk in Tris-buffered saline with 0.01% Tween 20 and incubated with the antibodies listed in Supplemental Table 4. Proteins of interest were visualized and quantified with the ChemiDoc XRS+ System and Image Lab software version 5.2.1 (Bio-Rad).

Targeted proteomic analysis

To determine protein levels of ApoB (ApoB48 and ApoB100) in plasma and isolated VLDL samples (isolated as described above), we used a targeted proteomic assay as previously described (35). For plasma samples, we selected 5 representative samples from each group. In-gel digestion was performed on 1 µl of plasma, and 22.5 µl of VLDL samples, and the amount of isotopically-labeled standards added for the quantification was optimized for each sample type. LC-MS analyses and data processing and quantification were done as previously reported (25).

Discovery-based (untargeted) proteomic analysis

Discovery-based proteomics was used to determine relative protein concentrations in whole liver samples and sucrose-fractionated liver samples. For whole liver samples, 6 representative samples were selected from each group. In-gel digestion was performed on 50

µg of liver lysates or 30 µl from the collected sucrose fractions as described previously (25), except that relative quantification (Label Free Quantification) based on the peak areas was done without the use of isotopically-labeled standard peptides.

For the whole liver lysates, the discovery-based proteomics analyses were performed as described previously (40). A rerun of the whole liver lysates was done with a digestion based on the published SP3 digestion protocol (41) using the discovery-based proteomics settings similar to the sucrose gradient samples, to detect SOAT2. For the SP3 digestion protocol, 10 µg of total protein was diluted in 100 mM ammonium bicarbonate to a final volume of 25 µl as starting material. Reduction was performed by adding 10 µl 10 mM dithiothreitol and incubation for 30 min at 57 ºC. Alkylation was done with 10 µl 30 mM iodoacetamide for 30 min at room temperature under aluminum foil. The proteins were bound to 10 µl prewashed beads (1:1 mix of hydrophilic and hydrophobic Cytiva SeraMag beads, Fisher Scientific), and the samples were diluted to 50% acetonitrile with 55 µl acetonitrile. After removal of the acetonitrile, the beads were was twice with 200 µl 80% v/v ethanol, once with 180 µl acetonitrile, and resuspended in 40 µl 2.5 ng/µl trypsin (V5111 sequencing grade modified trypsin, Promega) for overnight digestion at 37 ºC. The digestion was stopped by addition of 10 µl 1% v/v formic acid and an equivalent of 1 µg was loaded on the Evosep tips for the untargeted proteomics analyses.

For the sucrose gradient samples, the discovery mass spectrometric analyses were performed on a quadrupole orbitrap mass spectrometer equipped with a nano-electrospray ion source (Orbitrap Exploris 480, Thermo Scientific). Chromatographic separation of the peptides was performed by liquid chromatography (LC) on an Evosep system (Evosep One, Evosep) using a nano-LC column (EV1137 Performance column 15 cm x 150 µm, 1.5 µm, Evosep; buffer A: 0.1% v/v formic acid, dissolved in milliQ-H2O, buffer B: 0.1% v/v formic acid, dissolved in acetonitrile). Ten percent of the sucrose fraction digests were injected and separated using the 30SPD workflow (Evosep). The mass spectrometer was operated in positive ion mode and data-independent acquisition mode (DIA) using isolation windows of 16 m/z with a precursor

mass range of 400-1000, switching the FAIMS between CV-45V and -60V with three scheduled MS1 scans during each screening of the precursor mass range.

Raw LC-MS data were processed with Spectronaut (16.0.220606) (Biognosys) with the standard settings of the directDIA workflow except that quantification was performed on MS1 with a mouse SwissProt database (www.uniprot.org, 17021 entries). For data quantification of total livers, local normalization was applied, and the Q-value filtering was set to the classic setting without applying imputation. With these data, z-scores were calculated and used to construct a heatmap to visualize the relative expression of lysosomal proteins. Alternatively, data were used to express relative SOAT2 levels. For sucrose fractionated samples, the Q-value filtering was set to the classic setting without applying normalization or imputation, and the data were used to visualize the expression of proteins in each sucrose fraction, relative to the total protein expression in all fractions.

LAL activity assay

LAL activity was determined in control and VPS35-deficient Hepa1-6 cells using the LysoLive™ Lysosomal Acid Lipase Assay Kit (ab253380, Abcam) according to the manufacturer's instructions for adherent cells. Cells were incubated with LysoLive™ LipaGreen™ for 6 hours in serum-free medium prior to reading cells with flow cytometry. Cells were analyzed with the BD FACSVerse™ (BD, Biosciences). Data was processed with Kaluza software (Beckman Coulter).

Statistical analysis

Unless indicated otherwise, data are presented as mean ±SEM. Statistical analyses were performed with GraphPad version 9.1 (GraphPad software). Differences between 2 groups were determined with unpaired two-tailed Student's *t* test. For comparing two variables between groups, two-way ANOVA with Tukey's multiple comparison test was performed. In all cases, P values of < 0.05 were considered statistically significant.

Results

Liver-specific depletion of VPS35 increases hepatic cholesterol content

To examine the physiological role of Retromer in cholesterol homeostasis, we generated a liver-specific *Vps35* knockout (*Vps35*^{HepKO}) mouse model. Using immunoblotting, we confirmed the ablation of VPS35 in the livers of *Vps35*^{HepKO} mice (Figure 1A). In line with previous studies (42, 43), loss of VPS35 strongly decreased the protein levels of the other Retromer subunits VPS26 and VPS29 by 91% and 83%, respectively (Figure 1A,B). Retromer shares its subunit VPS29 with Retriever, which consists of VPS26C, VPS29, and VPS35L, and shows structural similarities with Retriever (44). Retriever is physically and functionally connected with the COMMD1/CCDC22/CCDC93 (CCC) complex(35, 44) and therefore we also determined the protein levels of VPS35L and the CCC components CCDC22, CCDC93 and COMMD1. The results show that hepatic loss of VPS35 did not affect the levels of these proteins (Figure S1A), indicating that the formation and stability of Retriever and CCC complex do not rely on VPS35.

Vps35^{HepKO} mice were born at the expected Mendelian ratio, but the body and liver weights of these animals were slightly higher compared to their wild-type littermates (Figure 1C). To determine the effect of hepatic *Vps35* depletion on hepatic lipid levels, we measured cholesterol and triglycerides (TG) in liver homogenates. Hepatic total cholesterol (TC) content in *Vps35*^{HepKO} mice was significantly increased compared to control mice (Figure 1D), while TG concentrations tended to decrease (Figure 1E). The increase in TC was caused by higher FC as well as CE (Figure 1D). Using lipidomics, we confirmed the increase in CE (+46%) and found a significant 26% decrease in hepatic TG levels (Figure 1F). In addition, we observed changes in other lipid species, including the sphingolipids sphingomyelin (SM) (-14%), dihydroceramide (DCer) (+31%), and lactosylceramide (LCer) (+193%), and the phospholipid lysophophatidylethanolamine (LPE), a minor component of cell membranes, which was elevated by 67% (Figure 1F).

The increase in hepatic cholesterol content was accompanied by elevated plasma levels of the liver enzymes alanine transaminase (ALT) and aspartate transaminase (AST)

(Figure 1G), suggesting that hepatic loss of VPS35 induces liver damage. However, histological examination using hematoxylin and eosin (H&E) and TUNEL staining did not reveal overt liver damage nor hepatocellular apoptosis, respectively (Figure S1B,C). In addition, we found an increase in the expression of the monocyte/macrophage marker *Cd68* and monocyte chemoattractant protein 1 (*Mcp1*), but no significant changes in the expression of other inflammatory markers, such as *Il1β*, *Il6*, *Tnf*, and *F4/80* (Figure 1H). Together, these findings show that the hepatic Retromer is essential to maintain hepatic cholesterol homeostasis.

Hepatic VPS35 deficiency leads to hypercholesterolemia

Considering that the liver and the endo-lysosomal system are essential to maintain plasma cholesterol concentrations (24–26, 35, 45, 46), we also determined plasma lipid levels in *Vps35*^{HepKO} and control mice. We noted that hepatic VPS35 deficiency resulted in a 36% increase in plasma cholesterol levels without affecting plasma TG levels (Figure 2A,B). Fast protein liquid chromatography (FPLC) separation showed that the elevated plasma cholesterol levels in *Vps35*^{HepKO} mice were mainly caused by an increase in LDL cholesterol (Figure 2C), which was supported by a two-fold increase in plasma levels of ApoB (Figure 2D). Thus, our data demonstrate an important role of hepatic Retromer in controlling plasma LDL cholesterol levels.

Hepatic loss of VPS35 increases the number of degradative compartments

VPS35 deficiency has previously been linked to changes in late endosomal/multivesicular bodies (MVBs) and lysosomal structure and aberrant lysosomal function and autophagy (42, 43, 47–49). To this end, we analyzed the ultrastructure of MVBs and the degradative compartments. This latter includes lysosomes and autolysosomes/amphisomes, using transmission electron microscopy (TEM). We found that the number of MVBs and degradative compartments was significantly increased in VPS35-deficient hepatocytes (Figure S1D, Figure 3A,B). Since degradative compartments are key to autophagy, we analyzed the impact of VPS35 deficiency on the protein level of the autophagic marker LC3. LC3-I and LC3-II levels

were both significantly increased in *Vps35*^{HepKO} livers (Figure 3C). To assess whether hepatic loss of VPS35 affects autophagic flux, we ablated *Vps35* in Hepa1-6 mouse hepatoma cells using CRISPR/Cas9-mediated gene editing and treated control and VPS35-deficient (VPS35-KO) cells with the autophagy inhibitor Bafilomycin A1. We observed that LC3-II levels increased over time in both control and VPS35-KO cells, indicating that autophagic flux is not impaired in cells lacking VPS35 (Figure S2A). These observations were supported by measurements in Hepa1-6 cells using an autophagic flux probe(37) upon shRNA-mediated downregulation of ATG7 (shATG7), an essential autophagy gene (50), or VPS35 (shVPS35) (Figure S2B). In contrast to shATG7 cells, in which the autophagic flux is blocked, starvation-induced autophagy in shVPS35 cells was comparable to control cells, with a 20% decrease in GFP/RFP ratio in both groups (Figure S2C,D). Blocking autophagic flux by Bafilomycin A1 treatment also had similar effects in shVPS35 and control cells (Figure S2D). These findings indicate that Retromer deficiency changes the number of degradative compartments without affecting autophagic flux.

Loss of hepatic VPS35 decreases the levels of a subset of lysosomal proteins involved in intracellular cholesterol transport

To obtain further insight into the impact of VPS35 deficiency on the lysosomal system, we analyzed the levels of a range of lysosomal proteins. Despite the increased number of degradative compartments, the protein levels of the LE/lysosomal marker LAMP1 were not different between *Vps35*^{HepKO} and control mice (Figure 3C). Next, we analyzed the levels of other LE/lysosomal proteins using proteomics. We found that LAMP2 and multiple other lysosomal proteins were unaffected by the loss of VPS35 (Figure 3D), while some were significantly increased, including the V-ATPase subunits v1c1 and v1b2 (VATC1 and VATB1), Cathepsin B (CATB), and NPC2 (Figure 3D), or markedly reduced, such as RAB7A and the lysosomal hydrolases TPP1, RISC, PPGB (also known as Cathepsin A), and LAL (Figure 3D). Interestingly, a 61% reduction was observed in the protein levels of SCARB2. NPC1 was not identified in the proteomic approach, but because of its essential role in lysosomal cholesterol

export, we determined its levels by immunoblotting. Surprisingly, NPC1 levels were decreased by 85% in *Vps35*^{HepKO} livers compared to controls (Figure 3E,F). We also confirmed the strong downregulation of SCARB2 levels as found with proteomics by immunoblotting (Figure 3E,F). In line with decreased protein levels of LAL, we found that LAL activity was significantly reduced in VPS35-KO cells compared to controls (Figure 3G). The changes in the protein levels of NPC1, NPC2, SCARB2, and LAL were all independent of changes at the mRNA level (Figure 3H), suggesting that the observed changes in the levels of these proteins are due to post-transcriptional events. Collectively, these data show that hepatic loss of Retromer has specific effects on a subset of lysosomal proteins, including key proteins required for cholesterol metabolism and transport, such as LAL, NPC1, and SCARB2.

Hepatic VPS35 deficiency increases hepatic cholesterol synthesis due to impaired endo-lysosomal cholesterol transport

To get insight into the relative distribution of NPC1, SCARB2, and LAL within endo-lysosomal compartments, sucrose density gradient fractionation of liver homogenates of *Vps35*^{HepKO} and control mice was performed. Using proteomics, we analyzed the proteome in the different fractions and detected the Retromer subunits mainly in fractions 5-7 in control livers (Figure S3A) and confirmed the marked reduction of the subunits upon *Vps35* ablation (Figure S3A). Next, we found that NPC1, SCARB2, and LAMP1 were primarily present in fractions 13-15 (Figure 4A). LAMP2 was also present in fractions 13-15, but was mainly detected in fractions 3-5, where it co-sedimented with LAL. NPC1, SCARB2, and LAL levels were decreased in most of the fractions derived from VPS35-deficient livers. Although the LAMP1 levels were unchanged, its relative distribution was shifted from fractions 13-15 to fractions 10-12 upon *Vps35* ablation (Figure 4A), which might indicate that the morphology of LAMP1-positive degradative compartments is changed.

To study the relative distribution of cholesterol, we measured the cholesterol content in the same fractions that were used for proteomics. We confirmed that loss of VPS35 increased hepatic cholesterol (Figure 4A and S3B) and found that this increase was mainly seen in

LAMP1/2, NPC1, and SCARB2-positive fractions (Figure 4A), suggesting that hepatic loss of VPS35 results in cholesterol accumulation in LE/lysosomes.

We next investigated whether hepatic loss of VPS35 affects whole-body cholesterol homeostasis by studying cholesterol fluxes in *Vps35*^{HepKO} and control mice (28). We administered D_7-labeled cholesterol orally, and measured enrichment of the tracer in the blood during 7 consecutive days (Figure 4B). The kinetic parameters of cholesterol-D_7 turnover were calculated by curve fitting, and we found that the rate of cholesterol-D_7 secretion by the liver into the circulation was markedly reduced in hepatic VPS35-deficient mice (Figure 4B,C) compared to controls. Yet, fractional intestinal cholesterol absorption was similar between the groups (Figure S3C). These data indicate that after receptor-mediated endocytosis of D_7-cholesterol-containing chylomicron remnants, hepatic secretion of chylomicron-derived cholesterol into the circulation is delayed in *Vps35*^{HepKO} mice compared to controls. This observation suggests that the transport of endocytosed cholesterol out of the lysosome to the ER is compromised upon hepatic *Vps35* ablation, which is in accordance with the observed cholesterol accumulation in LAMP1/2, NPC1, and SCARB2-positive fractions (Figure 4A).

The observed differences in cellular cholesterol distribution may have consequences for *de novo* cholesterol production. In NPC and LAL-D patient fibroblasts, and *Npc1*$^{-/-}$ and *Lal*$^{-/-}$ mice, it has been demonstrated that impaired lysosomal cholesterol egress is associated with increased SREBP-mediated cholesterol biosynthesis (5, 51–53). In line, using transcriptome analysis, we found that the SREBP2-driven cholesterol biosynthesis pathway is upregulated in our mice, with pronounced upregulation of genes including 3-hydroxy-3-methylglutaryl-CoA synthase 1 *(Hmgcs1),* mevalonate kinase *(Mvk)*, and squalene epoxidase *(Sqle)*, upon *Vps35* ablation (Figure 4D). To assess the possible functional consequences of these observations, we studied *de novo* cholesterol synthesis. To this end, we gave mice drinking water containing the labeled cholesterol precursor ^{13}C-acetate for 5 days and measured the incorporation of the tracer into cholesterol molecules from bloodspots. Mass isotopomer distribution analysis (MIDA) was then applied to calculate fractional cholesterol synthesis (29, 30). We found that loss of hepatic VPS35 significantly increased whole-body cholesterol synthesis rates (Figure

4E), which in mice predominantly reflects hepatic cholesterol synthesis (54). Together, these findings indicate that Retromer is essential for lysosomal cholesterol egress. In the absence of Retromer, the hepatocytes accumulate cholesterol in LE/lysosomes, which results in enhanced *de novo* cholesterol synthesis.

Hypercholesterolemia in Vps35^{HepKO} mice is associated with CE-enrichment of VLDL particles and impaired lipoprotein receptor transport

A recent study showed that patients with partial LAL deficiency (CESD), who are hypercholesterolemic, have CE-enriched VLDL particles (55). These CEs are derived from hepatic sterol O-acyltransferase 2 (SOAT2; also known as ACAT2) (55), an ER-resident enzyme responsible for cholesterol esterification yielding CE for incorporation in VLDL particles (56, 57). Given that *Vps35*^{HepKO} mice are also hypercholesterolemic (Figure 2A,C) and show increased hepatic *Soat2* mRNA levels (Figure 5A), we assessed whether this was associated with changes in SOAT2 protein levels and VLDL secretion and composition. Consistent with increased *Soat2* mRNA levels (Figure 5A), the hepatic protein levels of SOAT2 were elevated (Figure 5B). Next, we determined the VLDL-TG secretion rate in mice by measuring plasma TG levels at different time points after injection of the lipoprotein lipase (LPL) inhibitor P407. Although we did not find differences in VLDL secretion rate (Figure 5C), we did find that the lipid composition of VLDL particles (phospholipids (PL): cholesterol: triglycerides, corrected for total ApoB levels) was different between control and *Vps35*^{HepKO} mice (Figure 5D). The VLDL particles of *Vps35*^{HepKO} mice had a relatively higher cholesterol content compared to control mice (Figure 5D). Thus, hepatic loss of Retromer results in cholesterol-enriched VLDL particles.

Retromer is physically associated with the WASH complex, a pentameric protein complex that acts together with the CCC complex to recycle LDLR and LDLR-related protein 1 (LRP1) from the endosome back to the cell surface (24–26). Since hepatic depletion of either WASH or CCC reduces surface LDLR and LRP1 levels, accompanied by elevated plasma LDL cholesterol levels (24–26), we studied the hepatic levels of both receptors. We found that loss

of VPS35 resulted in a 50% increase in hepatic LDLR protein levels, and a 40% decrease in LRP1 levels (Figure 5E,F), without changes in the respective mRNA levels (Figure S4A). Although total LDLR levels were increased, sucrose density gradient fractionation showed that the relative distribution of LDLR was changed upon *Vps35* depletion (Figure 4A). In control livers, the majority of LDLR is present in fractions 13-14, while in *Vps35*^{HepKO} livers LDLR is mainly present in fractions 11-13 and co-sedimented with the lysosomal marker LAMP1 (Figure 4A). The relative distribution of LRP1 was also changed in VPS35-deficient livers. We found that the majority of LRP1 was detected in the LAMP1-positive fractions 11-13 (Figure 4A). To further explore the role of VPS35 in the endosomal transport of LDLR and LRP1, we studied the protein expression of these receptors in primary hepatocytes isolated from *Vps35*^{HepKO} and control mice. VPS35 deficiency strongly reduced the total protein levels of LDLR and LRP1 as well as their presence at the cell surface (Figure S4B). Since Retromer prevents cargos from lysosomal degradation by sorting them through the endo-lysosomal network (58), these data suggest that hepatic loss of Retromer impairs the endosomal transport of LDLR and LRP1, a defect that likely explains the elevated plasma LDL cholesterol levels in *Vps35*^{HepKO} mice (Figure 2A,C).

Reduced NPC1 and SCARB2 protein levels in Vps35^{HepKO} livers are not caused by increased proteolysis

To get mechanistic insight into how loss of VPS35 decreases NPC1 and SCARB2 levels, we cultured primary hepatocytes isolated from *Vps35*^{HepKO} and control mice. We first confirmed that VPS35 deficiency blunts NPC1 and SCARB2 protein levels (Figure 6A), a change that cannot be explained by changes in mRNA levels (Figure 6B). A previous study showed that NPC1 can be degraded when it fails to be trafficked from the ER towards the LE/lysosome or is misfolded due to mutations (59). NPC1 mutant proteins are either degraded via ER-phagy (selective autophagy of ER proteins), or ER-associated degradation (ERAD) through the proteasome system (60). To determine whether loss of VPS35 affects protein folding, we cultured primary hepatocytes of *Vps35*^{HepKO} and control mice at 30°C to improve the quality of

protein folding (61). However, lowering the temperature to 30°C did not improve NPC1 and SCARB2 protein expression compared to cells cultured at 37°C (Figure 6C).

To assess whether VPS35 deficiency promotes NPC1 proteolysis, we treated primary hepatocytes of *Vps35*^{HepKO} and control mice with the lysosomal inhibitor Bafilomycin A1 or the proteasomal inhibitor MG132. Consistent with previous findings (60), both treatments resulted in elevated levels of NPC1 and SCARB2 in control cells (Figure 6D), but they failed to normalize NPC1 or SCARB2 protein expression in *Vps35*^{HepKO} primary hepatocytes (Figure 6D). Thus, reduced levels of NPC1 and SCARB2 upon VPS35 deficiency are not caused by misfolding or enhanced proteolysis.

A high-fat, cholesterol-enriched diet (HFCD) exacerbates hypercholesterolemia in Vps35^{HepKO} mice

To further explore the role of hepatic Retromer in cholesterol homeostasis, we challenged *Vps35*^{HepKO} and control mice with a high-fat, cholesterol-enriched diet (HFCD) for 12 weeks, starting at 12 weeks of age. In contrast to standard diet-fed mice (Figure 1C), HFCD-fed *Vps35*^{HepKO} mice gained less body weight during the diet intervention compared to control mice (Figure 7A,B), which was mainly caused by a reduction in fat mass (Figure 7C). HFCD feeding exacerbated the hypercholesterolemic phenotype of *Vps35*^{HepKO} mice (Figure 7D,E), while plasma TG levels were not altered compared to control mice (Figure 7F). Thus, feeding *Vps35*^{HepKO} mice a HFCD worsens their hypercholesterolemic phenotype, but attenuates diet-induced body weight gain.

Hepatic VPS35 deficiency aggravates diet-induced hepatic cholesterol accumulation, accompanied by liver inflammation and hepatocellular proliferation

Although liver weights between HFCD-fed *Vps35*^{HepKO} and control mice were not different (Figure 8A), HFCD feeding exacerbated hepatic cholesterol accumulation in *Vps35*^{HepKO} mice (Figure 8B). Using lipidomics, we found that CE levels were increased by 52% in *Vps35*^{HepKO} compared to control livers (Figure S5A). Interestingly, hepatic VPS35 ablation resulted in a

50% reduction in hepatic TG levels after HFCD feeding (Figure 8C and S5A). In contrast, concentrations of several other lipid classes were significantly increased upon hepatic VPS35 ablation, including those of sphingolipids, such as ceramide (Cer) (+12%), dihydroceramide (DCer) (+56%), hexosylceramide (HCer) (+43%) and sphingomyelin (SM) (+23%), the phospholipids lysophosphatidylcholine (LPC) (+39%) and lysophosphatidylethanolamine (LPE) (+30%), and free fatty acids (FFA) (+24%) (Figure S5A). Histological examination upon H&E staining revealed that control livers mainly showed micro- and macrovesicular accumulation of lipids located around the central vein (pericentral), whereas VPS35-deficient livers presented large lipid vacuoles without clear zonation (panzonal) (Figure 8D). Histological examination also indicated infiltration of inflammatory cells in *Vps35*^{HepKO} livers (Figure 8D). We found an increase in the numbers of macrophages and infiltrated monocytes in *Vps35*^{HepKO} livers compared to controls, as determined by immunohistochemical staining for F4/80 and CD11b, respectively (Figure 8D and S5B). The mRNA expression of the inflammatory markers *Cd68, Mcp1*, and *Tnf* was also increased (Figure 8E), and the infiltration of B-cells (B220) and T-cells (CD3) was slightly elevated in VPS35-deficient livers as well (Figure S5B). Furthermore, this inflammatory phenotype in *Vps35*^{HepKO} mice was accompanied by a mild increase in liver fibrosis, as shown by immunohistochemical staining for collagen using Sirius Red (Figure 8D), as well as by increased mRNA expression of the fibrotic markers *Col1* and *Timp1* (Figure 8F). We found no marked changes in the number of CK19-positive cholangiocytes, suggesting that hepatic VPS35 deficiency and HFCD-feeding does not lead to a ductular reaction (Figure S5B). However, we did find that the number of Ki67 and BrdU-positive hepatocytes, both markers for cell proliferation, were significantly increased (Figure 8D,G and S5B). Furthermore, the plasma levels of liver enzymes ALT and AST were elevated in HFCD-fed *Vps35*^{HepKO} mice compared to control mice (Figure S5C). Taken together, here we show that hepatic Retromer is essential to maintain hepatic cholesterol homeostasis and prevents liver injury when mice are challenged with HFCD.

Discussion

Retromer (VPS35-VPS26-VPS29) is a central player of the endo-lysosomal network that facilitates the transport of cargos from endosomes to the trans-Golgi network (TGN) or the plasma membrane and protects them from lysosomal proteolysis (15–18). Retromer dysfunction is linked to Alzheimer's (AD) and Parkinson's disease (PD) (62–64), but various studies have insinuated that Retromer may also control cholesterol homeostasis (19, 22). However, its functional contribution to maintaining cholesterol homeostasis is unknown. To our knowledge, this is the first study showing that Retromer plays a key role in lysosomal cholesterol egress by controlling the protein levels of the lysosomal proteins LAL, SCARB2, and NPC1 in hepatocytes. In addition, Retromer is essential for maintaining plasma cholesterol levels, likely by facilitating the endosomal recycling of LDLR and LRP1.

We show that hepatic Retromer is an important protein complex for normal protein expression of LAL, SCARB2, and NPC1, as VPS35 ablation markedly reduces the levels and function of these lysosomal proteins. In line with the phenotypes of LAL-D and NPC disease (MIM #613497, #620151, #278000, #257220, #607625), dysfunction of these proteins is accompanied by CE and FC accumulation, likely in LE/lysosomal compartments due to compromised CE hydrolysis and lysosomal cholesterol egress, respectively. Furthermore, reduced lysosomal cholesterol egress in NPC disease and LAL-D is associated with increased cholesterol biosynthesis (5, 51–53), a phenotype that we also observed in hepatic VPS35-deficient mice and is probably due to impaired movement of cholesterol out of the lysosomes to the ER, which subsequently results in enhanced activation of the SREBP2-activated cholesterol biosynthetic pathway.

The underlying mechanism of how VPS35 depletion reduces the levels of LAL, SCARB2, and NPC1, remains unclear. LAL is a lysosomal luminal protein, and modification of LAL with mannose-6-phosphate (M6P) in the TGN is required for its efficient targeting to the lysosomes, as for many lysosomal soluble proteins (65). Retromer regulates the retrograde transport of CI-M6PR from the endosome back to TGN (20, 21), and since CI-M6PR is one of

the two receptors that transport M6P-modified proteins to the lysosomes (66), it is plausible that loss of VPS35 indirectly impairs the transport of LAL from the TGN to the lysosomes. This defect in LAL sorting might result in increased LAL secretion from the biosynthetic pathway, similar to what has been reported for Cathepsin D (42, 67–69).

Alternatively, the reduced levels of LAL, NPC1, and SCARB2 might be the result of increased lysosomal exocytosis or release of extracellular vesicles (EV), such as exosomes, which contain various proteins, nucleic acids, and lipids (70). Increased lysosomal exocytosis and release of exosomes are frequently seen when lysosomal function is impaired, probably to protect cells and maintain cellular homeostasis (70–74). Similar observations are made when lysosomal dysfunction is chemically induced, e.g. with Bafilomycin A1 (75, 76). Bafilomycin A1 is also frequently used to block lysosomal degradation of proteins. However, NPC1 and SCARB2 levels could not be normalized when primary VPS35-deficient hepatocytes were treated with this drug or by blocking proteasomal degradation, and since the mRNA levels of *Npc1* and *Scarb2* in hepatic VPS35-deficient mice do not explain the reduced NPC1 and SCARB2 protein levels, one can hypothesize that loss of Retromer induces EV-mediated secretion of NPC1 and SCARB2.

Interestingly, increased numbers of the degradative compartment amphisomes have been linked to increased secretion of EVs (77, 78). Amphisomes are formed by the fusion of autophagosomes with late endosomes or multivesicular bodies (MVBs). They contain typical autophagosome markers, such as lipidated LC3 (LC3-II), and can fuse with the plasma membrane for EV secretion (77, 78). Because it is very challenging to distinguish different degradative compartments, we can currently not provide evidence that VPS35 deficiency results in an increased number of amphisomes. However, we found that the number of MVBs and degradative compartments and the levels of LC3-II are all elevated in VPS35-deficient hepatocytes. These data may suggest that the number of amphisomes is also increased, similar to what has been previously shown in VPS35-deficient Drosophila larval fat body cells (48). Moreover, Retromer has been associated with exosome biogenesis (79), which further supports our hypothesis that loss of Retromer results in increased secretion of EVs. Although

Retromer and lysosomal dysfunction have been linked to aberrant autophagic flux (80), we could not find evidence that autophagic flux in hepatocytes is affected in the absence of VPS35, which suggests another role for Retromer in the interactions between the endocytic compartment, lysosomes, and autophagosomes in hepatocytes.

A critical role of Retromer in endo-lysosomal pathway function has also been observed in H4 neuroglioma cells by Daly and colleagues (49). They found that Retromer dysfunction causes mislocalization of many different lysosomal membrane proteins, including LAMP1, LAMP2 and NPC1. Although these lysosomal proteins were mainly mislocalized at the cell surface of VPS35-deficient cells, their total levels were not altered as we found for NPC1 in our study (49). Furthermore, they also showed that loss of VPS35 is associated with increased lysosomal exocytosis of lysosomal lumen proteins, including LAL, NPC2, and various cathepsins (e.g. CATA, CATB, CATD, CATL), which was explained by lysosomal dysfunction (49). Although the total levels of LAL and CATD are also reduced in VPS35-deficient livers, we found that NPC2 and CATB are both elevated upon hepatic VPS35 ablation. Previous studies in NPC fibroblasts have shown that the loss of NPC1 leads to a compensatory upregulation of NPC2 (81–83), which might explain the increased NPC2 protein levels in our model. The reason for the inconsistencies between Daly's and our study remains unknown, but it could be explained by the different model systems and tissues that were examined. Further experiments, such as isolation and proteomic characterization of the exosomes of wild-type and VPS35-deficient cells, are needed to uncover the mechanisms of how hepatic Retromer affects the levels of LAL, SCARB2, and NPC1.

Our study also shows that *Vps35*^{HepKO} mice have elevated plasma LDL-cholesterol levels. We show that increased hepatic SOAT2 expression in *Vps35*^{HepKO} mice is associated with cholesterol-enrichment of VLDL particles, similar to what has previously been found in LAL-D patients (55). Importantly, however, hypercholesterolemia in *Vps35*^{HepKO} mice is likely mainly due to impaired hepatic uptake of cholesterol by LDLR and LRP1 (84, 85). Although we did not find an effect on the protein levels and relative distribution of WASH and CCC components (Figure S3A), it has been shown that Retromer is associated with the WASH and

CCC complexes to recruit both complexes to the endosome (23, 86, 87). Both multimeric protein complexes coordinate endosomal recycling of cargos including LDLR and LRP1 (25, 26). In contrast to hepatic loss of WASH or CCC (25, 26), hepatic VPS35 ablation increases hepatic protein levels of LDLR by 50% while reducing LRP1 levels by 40%. These changes in protein levels cannot be explained by their mRNA levels, suggesting that post-transcriptional events are driving these effects. Given that upregulation of LDLR at the protein level occurs as a compensatory mechanism for impaired LRP1 functioning (35, 39, 85, 88, 89), these data may indicate that VPS35 deficiency only disturbs the function of LRP1 but not that of LDLR. However, impaired hepatic function of only LRP1 does not result in increased LDL-cholesterol levels (35, 85, 88), suggesting that hepatic VPS35 deficiency may also affect LDLR function. Indeed, we show that the relative distribution of LDLR within endo-lysosomal compartments is changed upon VPS35 deficiency; LDLR is highly enriched in fractions positive for the lysosomal marker LAMP1. Daly *et al*. also found that loss of VPS35 results in an enrichment of LDLR and LRP1 in lysosomes (49). Furthermore, we found that VPS35 deficiency in primary hepatocytes leads to reduced total and surface levels of LDLR and LRP1, likely due to impaired retrieval of these cargos from the lysosomal degradation pathway (58). Thus, although total LDLR levels are increased upon hepatic VPS35 ablation, we cannot rule out that missorting of LDLR to endo-lysosomal compartments occurs, leading to impaired recycling of LDLR from endosomes back to the cell surface and, consequently, reduced hepatic LDL-cholesterol uptake.

It is important to note that impaired Retromer function has been associated with various neurodegenerative diseases. VPS35 levels are decreased in brain regions of patients with Alzheimer's disease (AD) (62), in which Retromer dysfunction is associated with accumulation of MAPT/Tau and Amyloid beta (Aβ) (43, 90–92). Furthermore, the *VPS35*-D620N mutation is causative for an autosomal dominant form of Parkinson's disease (PD) (63, 64). Although it is currently unclear whether this mutation is associated with disturbances in whole-body cholesterol homeostasis (e.g. hypercholesterolemia), previous studies have demonstrated that cholesterol homeostasis is often affected in neurodegenerative diseases (93–95). Thus, it is

tempting to speculate that Retromer dysfunction may also contribute to disturbed cholesterol homeostasis in the brain of AD and PD patients, besides its established role in endosomal sorting of receptors and autophagy in neurons (43, 90–92).

We also show that HFCD-feeding aggravated hepatic and plasma cholesterol levels in *Vps35*^{HepKO} mice compared to control mice. Similar to hepatic LAL-deficient mice (96), this is associated with increased liver inflammation and liver damage. Interestingly, we also found elevated hepatocellular proliferation in livers of HFCD-fed *Vps35*^{HepKO} mice. It is known that cholesterol metabolism plays an important role in development of cancers, including hepatocellular carcinoma (HCC) (97–99). Currently, it is unclear whether the increased proliferation is a direct effect of VPS35 deficiency or a consequence of disturbed cholesterol homeostasis in *Vps35*^{HepKO} mice. Importantly, in contrast to our findings, a previous report dubbed *VPS35* as an oncogene in HCC (100). Hence, to elucidate the role of VPS35 in hepatocellular proliferation and HCC development, additional studies are required.

Taken together, we identified hepatic Retromer as a central player in cholesterol homeostasis. In addition to the well-established role of Retromer in endosomal sorting of cargos, we uncovered its importance in lysosomal cholesterol egress by controlling the levels and function of the lysosomal proteins LAL, SCARB2, and NPC1.

Acknowledgements

The authors would like to acknowledge Niels Mulder, Desi Tsoneva, Trang Le and Martijn Koehorst for their technical assistance with experiments, Ben Giepmans and Kim Kats for their assistance with EM, and Wouter Lamers for providing the CK19 antibody. In addition, we thank Katharina Kuentzel and Dagmar Kratky for their valuable input and suggestions.

This study was financially supported by grants from the European Union (MSCA-ITN-2020, 953489; Acronym EndoConnect) coordinated by B.v.d.S.; The Netherlands Cardiovascular Research Initiative: 'the Dutch Heart Foundation, Dutch Federation of University Medical Centers, The Netherlands Organization for Health Research and Development and the Royal Netherlands Academy of Sciences' (CVON2017-2020; Acronym Genius2) to J.A.K. and B.v.d.S.; ZonMW OC grant (2471032) to J.A.K. and B.v.d.S.; NWO ENW grant (OCENW.M.22.034) to B.v.d.S.; The Netherlands Organization for Scientific Research (VICI grant 016.176.640) to J.W.J; the Graduate School for Drug Exploration (GUIDE); and the De Cock-Hadders Foundation to D.V.; J.A.K. is an established investigator of the Netherlands Heart Foundation (2015T068). Electron Microscopy was performed in the UMCG Microscopy and Imaging Center (UMIC), sponsored by the Netherlands Organization for Scientific Research (ZonMW 91111.006; Ben Giepmans); and the Netherlands Electron Microscopy Infrastructure (NEMI), NWO National Roadmap for Large-Scale Research Infrastructure of the Dutch Research Council (NWO 184.034.014; Ben Giepmans).

Author contributions

D.Y.V. and B.v.d.S. conceived the study. D.Y.V., M.G.B., A.H.H., W.A.R.O., and J.J.T. performed the experiments with technical support from M.S., N.H., N.J.K., and R.H. M.H.K. performed histological stainings. F.K. and J.F.d.B. assisted in the design of the cholesterol flux experiment, and J.F.d.B. analyzed the data. B.v.d.S., F.R., and M.M. analyzed the EM data. M.M.F., L.S., and J.H. performed lipidomics analysis. J.C.W. performed and analyzed the proteomics experiments. D.Y.V., J.W.J., J.A.K., and B.v.d.S acquired financial support. J.A.K.

and B.v.d.S. supervised work. D.Y.V. and B.v.d.S analyzed and interpreted data and wrote the initial manuscript with all authors editing and approving the final text.

Declaration of interests

The authors declare that they have no conflicts of interest.

Figure legends

Figure 1. Hepatic *Vps35* depletion increases hepatic cholesterol content in mice. (**A**) Hepatic protein levels of the Retromer subunits VPS35, VPS26, and VPS29, determined by immunoblotting (n=4). (**B**) Quantification of hepatic protein levels of the Retromer subunits, as determined by immunoblotting (n=7). (**C**) Body and liver weights of WT and *Vps35*^{HepKO} male mice at 18 weeks of age (n=9). (**D**) Hepatic cholesterol (n=7-9) and (**E**) triglyceride (n=9) levels in WT and *Vps35*^{HepKO} male mice. (**F**) Concentrations of lipid classes in livers of WT and *Vps35*^{HepKO} male mice, determined by lipidomics analysis (n=7-9). (**G**) Plasma levels of ALT and AST (n=8-9). (**H**) Relative hepatic mRNA levels of inflammatory markers (n=9). Data are presented as mean ± SEM; * $p < 0.05$, ** $p < 0.01$ and *** $p < 0.001$. *Abbreviations: ALT = alanine transaminase; AST = aspartate transaminase; CE = cholesterol ester; Cer = ceramide; DCer = dihydroceramide; DG = diacylglycerol; FC = free cholesterol; FFA = free fatty acid; HCer = hexosylceramide; LCer = lactosylceramide; LPC = lysophosphatidylcholine; LPE = lysophosphatidylethanolamine; PC = phosphatidylcholine; PE = phosphatidylethanolamine; SM = sphingomyelin; TC = total cholesterol; TG = triacylglycerol.*

Figure 2. Liver specific VPS35-deficient mice are hypercholesterolemic. (**A**) Plasma cholesterol and (**B**) triglyceride levels in WT and *Vps35*^{HepKO} male mice (n=9). (**C**) Cholesterol levels in plasma fractionated by FPLC (n=7). (**D**) Protein levels of ApoB in plasma, determined by targeted proteomics (n=5). Data are presented as mean ± SEM; ** $p < 0.01$ and *** $p < 0.001$.

Figure 3. Hepatic loss of VPS35 affects the levels of various lysosomal proteins, including cholesterol transporters. (**A**) Scanning transmission electron microscopic images of livers of WT and *Vps35*^{HepKO} male mice, where amphisomes, autolysosomes, and lysosomes are indicated. Full datasets are available upon request. (**B**) Quantification of degradative compartments WT and *Vps35*^{HepKO} hepatocytes. (**C**) Immunoblot of LAMP1 and LC3 in livers

of WT and *Vps35*^{HepKO} male mice (n=4). (**D**) Heatmap showing z-scores of protein levels of LE/lysosomal proteins, presented as protein names, calculated from raw counts measured with untargeted proteomics (n=5); significantly changed proteins are indicated in bold and with *. (**E**) Immunoblot of NPC1 and SCARB2 in WT and *Vps35*^{HepKO} livers (n=4). (**F**) Quantification of NPC1 and SCARB2 protein levels (n=4) determined by immunoblotting. (**G**) LAL activity, expressed as mean fluorescence intensity, in WT and VPS35-KO Hepa1-6 cells, determined by FACS analysis (n=5 from two independent experiments). (**H**) Relative mRNA expression of *Npc1*, *Npc2*, *Scarb2,* and *Lipa* in WT and *Vps35*^{HepKO} male livers (n=9). Unless indicated otherwise, data are presented as mean ± SEM; *** $p < 0.001$.

Figure 4. Hepatic secretion of endocytosed cholesterol is impaired, while cholesterol biosynthesis is increased in *Vps35*^{HepKO} mice. (**A**) Relative distribution of various cholesterol transporters/receptors within the endo-lysosomal system as determined by sucrose gradient fractionation and proteomics. Cholesterol levels in the sucrose gradient fractions of WT and *Vps35*^{HepKO} liver homogenate, determined by Amplex™ Red cholesterol assay. Protein and cholesterol levels are presented as the percentage of total levels in all WT fractions. (**B**) Fractional enrichment of orally administered cholesterol-D_7 in WT and *Vps35*^{HepKO} mice (n=6-8). (**C**) Kinetic parameter *k3* describing the rate of cholesterol-D_7 secretion by the liver into the circulation in WT and *Vps35*^{HepKO} male mice (n=6-8). (**D**) Heatmap presenting the z-score normalized expression of genes in the cholesterol biosynthesis pathway in livers of WT and *Vps35*^{HepKO} male mice (n=6). (**E**) Fractional cholesterol synthesis in WT and *Vps35*^{HepKO} mice (n=8). Data are presented as mean ± SEM; * $p < 0.05$.

Figure 5. Loss of hepatic VPS35 changes VLDL composition and lipoprotein receptor levels. (**A**) Relative mRNA levels of hepatic *Soat2* in WT or *Vps35*^{HepKO} male mice (n=6), determined by RNAseq analysis. (**B**) Relative SOAT2 protein expression in WT and *Vps35*^{HepKO} livers (n=5), determined by proteomics. (**C**) Plasma triglyceride levels (n=6-8) in WT or *Vps35*^{HepKO} male mice, after IP injection with poloxamer 407. (**D**) VLDL particle

composition in WT and *Vps35*^{HepKO} male mice (n=3). TC, TG, and PL are presented as percentage of total lipids corrected for total ApoB levels; ApoB48 and ApoB100 are presented as percentage of total ApoB levels. * $p < 0.05$ and # $p < 0.01$. (**E**) Immunoblot of LDLR and LRP1 (n=4) in livers of WT and *Vps35*^{HepKO} mice. (**F**) Quantification of hepatic LDLR and LRP1 protein levels, determined by immunoblotting (n=7). Except for (**D**), data are presented as mean ± SEM with ** $p < 0.01$ and *** $p < 0.001$.

Figure 6. Reduced NPC1 and SCARB2 levels in *Vps35*^{HepKO} mice are not caused by increased proteolysis. (**A**) Protein levels of NPC1 and SCARB2 in primary hepatocytes isolated from WT and *Vps35*^{HepKO} mice (n=2). (**B**) Relative mRNA expression of *Npc1* and *Scarb2* in primary hepatocytes isolated from WT and *Vps35*^{HepKO} mice (n=2). (**C**) Immunoblot of NPC1 and SCARB2 in WT and VPS35-deficient primary hepatocytes cultured at 37°C or 30°C. (**C**) Immunoblot of NPC1 and SCARB2, non-treated (0) or treated with 100nM Bafilomycin A or 10μM MG132 for 10 and 22 hours. Data are presented as mean ± SEM; ** $p < 0.01$.

Figure 7. High-fat cholesterol-enriched diet (HFCD) feeding reduces body weight gain but increases hypercholesterolemia in *Vps35*^{HepKO} male mice. (**A**) Body weight of WT and *Vps35*^{HepKO} male mice, prior to and during HFCD feeding (n=7-9). (**B**) Body weight gain presented as % of BW at the start of HFCD feeding (n=7-9). (**C**) Lean, fat, and fluid mass for WT and *Vps35*^{HepKO} male mice after 12 weeks of HFCD feeding (n=7-9). (**D**) Plasma cholesterol after 12-week HFCD feeding (n=7-9). (**E**) Cholesterol levels after 12-week HFCD feeding, in pooled plasma fractionated by FPLC (n= one pooled sample from 7 WT or 9 *Vps35*^{HepKO} male mice). (**F**) Plasma triglyceride levels after 12-week HFCD feeding (n=7-9). Data are presented as mean ± SEM; * $p < 0.05$, ** $p < 0.01$ and *** $p < 0.001$.

Figure 8. HFCD feeding increases hepatic cholesterol levels, inflammation, and hepatocellular proliferation in *Vps35*^{HepKO} male mice. (**A**) Liver weights of HFCD-fed WT

and *Vps35*^{HepKO} mice (n=7-9). (**B**) Hepatic cholesterol and (**C**) triglyceride levels in WT and *Vps35*^{HepKO} male mice (n=7-9). (**D**) Representative images of H&E, F4/80, Sirius Red, and Ki67 stainings of liver sections from HFCD-fed WT and *Vps35*^{HepKO} male mice; scale bars represent 100µm. (**E**) Relative mRNA levels of inflammatory markers and (**F**) fibrotic markers, in livers of HFCD-fed WT or *Vps35*^{HepKO} male mice (n=7-9). (**G**) Quantification of Ki67^{+} and BrdU^{+} cells from images shown in **D** and Figure **S5B** (n=7-9). Data are presented as mean ± SEM; * $p < 0.05$; ** $p < 0.01$ and *** $p < 0.001$.

Supplemental Figure Legends

Figure S1. Hepatic VPS35 deficiency does not affect Retriever and CCC complex and does not lead to severe liver damage. (**A**) Protein levels of retriever and CCC complex subunits in WT and *Vps35*^{HepKO} male livers (n=4), determined by immunoblotting. (**B**) Representative images of H&E and TUNEL staining of liver sections from WT and *Vps35*^{HepKO} male mice; scale bars represent 100µm. (**C**) Quantification of TUNEL^{+} cells from images shown in **B** (n=6). (**D**) Quantification of multivesicular bodies (MVBs) per WT and *Vps35*^{HepKO} hepatocytes, data are presented as mean ± SEM.

Figure S2. Hepatic VPS35 ablation does not impair autophagic flux. (**A**) Immunoblot of LC3-I and II in control and VPS35-deficient Hepa1-6 cells treated with the autophagy inhibitor Bafilomycin (100nM) for indicated time points. (**B**) Immunoblot of GFP-LC3-RFP-LC3ΔG-expressing Hepa1-6 cells after shRNA-mediated downregulation of ATG7 or VPS35. (**C**) Autophagic flux in GFP-LC3-RFP-LC3ΔG-expressing Hepa1-6 cells deficient for ATG7 or VPS35, under non-starved or starved conditions; presented as GFP/RFP fluorescence ratio relative to non-starved EV-control cells. (n=2 from two independent experiments). (**D**) Autophagic flux in GFP-LC3-RFP-LC3ΔG-expressing Hepa1-6 cells deficient for VPS35 in non-starved or starved conditions or treated with 100nM Bafilomycin; presented as GFP/RFP fluorescence ratio relative to non-starved EV-control cells (n=3). Data are presented as mean ± SEM; * $p < 0.05$ and *** $p < 0.001$.

Figure S3. Loss of hepatic VPS35 does not negatively impact the distribution of hepatic endosomal sorting complexes, nor intestinal cholesterol absorption. (**A**) Relative distribution of retromer, retriever, CCC, and WASH subunits in WT and *Vps35*^{HepKO} liver homogenates determined by sucrose gradient fractionation and proteomics; presented as the percentage of total protein levels of all WT fractions. (**B**) Mean cholesterol concentrations determined by Amplex™ Red Cholesterol Assay in sucrose fractions of WT and *Vps35*^{HepKO}

liver homogenates. (**C**) Fractional intestinal cholesterol absorption in WT and *Vps35*^{HepKO} mice (n=6-8), data are presented as mean ± SEM.

Figure S4. Hepatic loss of VPS35 reduces total and surface protein levels of LDLR and LRP1. (**A**) Relative mRNA levels of hepatic *Ldlr* and *Lrp1* in WT and *Vps35*^{HepKO} male mice (n=9). (**B**) Protein levels of LDLR and LRP1 in whole-cell extracts and at the cell surface of WT and VPS35-deficient primary hepatocytes (n=3), determined by immunoblotting.

Figure S5. HFCD feeding increases hepatic CE levels, liver inflammation, and hepatocellular proliferation in *Vps35*^{HepKO} mice. (**A**) Concentrations of lipid classes in livers of WT and *Vps35*^{HepKO} male mice after 12-week HFCD feeding, determined by lipidomics analysis (n=6-9). (**B**) Representative images of CD11b, B220, CD3, CK19, and BrdU staining of liver sections from HFCD-fed WT and *Vps35*^{HepKO} male mice; scale bars represent 100µm. (**C**) Plasma levels of ALT and AST (n=7-9). Data are presented as mean ± SEM; * $p < 0.05$, ** $p < 0.01$ and *** $p < 0.001$. *Abbreviations: CE = cholesterol ester; Cer = ceramide; DCer = dihydroceramide; DG = diacylglycerol; FFA = free fatty acid; HCer = hexosylceramide; LCer = lactosylceramide; LPC = lysophosphatidylcholine; LPE = lysophosphatidylethanolamine; PC = phosphatidylcholine; PE = phosphatidylethanolamine; SM = sphingomyelin; TG = triacylglycerol.*

Supplemental Tables

Supplemental Table 1. Antibodies used for immunohistochemical analysis.

Target	Company	Catalog #	Dilution
B220	Santa Cruz	Sc-19597	1:100
BrdU	Dako	M0744	1:800
CD3	Dako	A0452	1:250
CD11b	Abcam	Ab133357	1:6000
CK19	*		1:600
F4/80	Abcam	Ab6640	1:500
Ki67	Thermofisher	RM-9106	1:50
Goat anti-rabbit (biotinylated)	Vector	BA-1000	
Goat anti-mouse (biotinylated)	Vector	BA-9200	
Goat anti-rat (biotinylated)	Vector	BA-9400	

** The anti-CK19 antibody was generated by W.H. Lamers, Academic Medical Center, Amsterdam, the Netherlands.*

Supplemental Table 2. Sequence of the sgRNAs and shRNAs used in the current study.

Gene		Sequence (5'-3')
Vps35	sgRNA #1	CACTCACCATGGCGACTCCG
	sgRNA #2	CCGGAGCTCTCCAAGCATAT
	sgRNA #3	CCAATATGCTTGGAGAGCTC
Vps35	shRNA#1	CTGGAGCAGGTTGTGAATTGTAG
	shRNA #2	AGGGGTTTGTTTCTTCGAAAT
Atg7	shRNA	CAGCCTCTGTATGAATTTGAA

Supplemental Table 3. Sequence of the primers used for qRT-PCR analysis.

Gene	Forward primer (5'-3')	Reverse primer (5'-3')
Cd68	TGACCTGCTCTCTCTAAGGCTACA	TCACGGTTGCAAGAGAAACATG
F4/80	TGTGTCGTGCTGTTCAGAACC	AGGAATCCCGCAATGATGG
Il1b	TGCAGCTGGAGAGTGTGG	TGCTTGTGAGGTGCTGATG
Il6	CTGCAAGAGACTTCCATCCAGTT	AGGGAAGGCCGTGGTTGT
Lipa	TGTTCGTTTTCACCATTGGGA	CGCATGATTATCTCGGTCACA
Ldlr	TCCAATCAATTCAGCTGTGG	GAGCCATCTAGGCAATCTCG
Lrp1	GACCAGGTGTTGGACACAGATG	AGTCGTTGTCTCCGTCACACTTC
Mcp1	GCTGGAGAGCTACAAGAGGATCA	ACAGACCTCTCTCTTGAGCTTGGT
Npc1	TGTTTGGTATGGAGAGTGTGGA	GTCACAGCAGAGACTGACATTG
Npc2	AGGACTGCGGCTCTAAGGT	AGGCTCAGGAATAGGGAAGGG
Ppia	TTCCTCCTTTCACAGAATTATTCCA	CCGCCAGTGCCATTATGG
Scarb2	AGAAGGCGGTAGACCAGAC	GTAGGGGGATTTCTCCTTGGA
Tnf	GTAGCCCACGTCGTAGCAAAC	AGTTGGTTGTCTTTGAGATCCATG

Supplemental Table 4. Antibodies used for immunoblot analysis.

Target	Company	Catalog #	Dilution
ATG7	Sigma	A2856	1:1000
β-actin	Sigma	A5441	1:1000
CDCC22	Proteintech	16636-1-AP	1:1000

CDCC93	Proteintech	20861-1-AP	1:1000
COMMD1	Proteintech	11938-1-AP	1:1000
HSP90	Cell Signaling	4874	1:1000
LAMP1	BioLegend	121602	1:1000
LC3	Cell Signaling	2775	1:1000
LDLR	Abnova	PAB8804	1:1000
LRP1	Abcam	ab92544	1:1000
NPC1	Invitrogen	PA1-16817	1:1000
SCARB2	Cell Signaling	27960	1:1000
Vinculin	Cell Signaling	4650	1:1000
VPS26	Abcam	ab23892	1:1000
VPS29	Abcam	ab98929	1:1000
VPS35	Abcam	ab10099	1:1000
VPS35L	Thermofisher	PA5-28553	1:1000
goat anti-mouse IgG (H+L)-HRP conjugate	Bio-Rad	170-6516	1:10000
goat anti-rabbit IgG (H+L)-HRP conjugate	Bio-Rad	170-6515	1:10000

Supplemental Methods

Transfection of Hek293T cells for production of γ-retroviral particles

HEK293T packaging cells were seeded in a 10 cm standard tissue culture dish to reach a confluency of 80%. Transfection of cells was performed using 7.0 µg of retroviral transfer plasmid pMRX-IP/GFP-LC3-RFP-LC3ΔG (kindly provided by Noboru Mizushima; Addgene plasmid #84572; http://n2t.net/addgene:84572; RRID:Addgene_84572)(37), 7.5 µg pGag/Pol, 2.5 µg pVSV-G packaging vectors and 1 µg pAdvantage expression enhancer. The plasmid mix was added to PEI (23966-2, Polysciences Inc.) transfection reagent prepared in Opti-MEMTM Reduced Serum Medium (31985062, Gibco) at 1:5 ratio (plasmid DNA Mix:PEI). The final mix was added to HEK293T cells dropwise. Media from viral particles producing-cells (10ml) was collected after 24h and 48h post-transfection and filtered through a 0.45 µm SFCA filter (431220, Corning). Finally, 0.5 µl of polybrene (4mg/ml stock concentration) (H9268-5G, Sigma) per ml of media was added to enhance retroviral transduction.

Generation of stable Hepa 1-6 cells expressing the autophagic flux probe

Hepa 1-6 cells were seeded in a 6-well plate 1 day before transduction and kept in the incubator at 37°C and 5% CO_2. Cells were transduced with 2ml of retroviral supernatant and incubated for 48h. Next day and 48h after transduction cells were checked for positive GFP and RFP expression by fluorescence microscopy. After 48h post-transduction, cells were harvested and expanded for two consecutive passages. The transduced Hepa 1-6 cells were maintained in DMEM GlutaMAX (Gibco) media supplemented with 10%FCS, 1% p/s and 2µg/ml puromycin. The cells generated in this step were considered polyclonal stable Hepa 1-6 cells expressing the autophagic flux probe GFP-LC3-RFP-LC3ΔG. In order to produce single monoclonal Hepa 1-6 cells that properly express the autophagic flux probe GFP-LC3-RFP-LC3ΔG (double positive cells) and exclude homologous recombination during the transfection and transduction procedures reported by Kaizuka *et al*., 2016(37), we sorted the polyclonal cells. In short, polyclonal Hepa 1-6 cells were harvested and kept on ice in FACS buffer containing 1X HBSS,

2%FCS, 2%BSA, 1%P/S. Cell sorting was performed using the MoFlo Astrios EQ Cell Sorter (Beckman Coulter, Life sciences) with a 100 μm nozzle equipped with the 488 nm and 561 nm lasers. Sort rate was set up to 25.000 events/sec and individual sort mode was used. Single double positive (GFP/RFP) cells were dripped in 96-well plates previously filled with 200 μL of standard cultured media supplemented with 2μg/ml puromycin. A total of three 96-well plates were filled with single double positive-cells to increase the chance of colonies growing. Sorted cells in 96-well plates were followed for the formation of single colonies with homogenous shape for not longer than 12 days; wells with more than one colony were discarded. Seven colonies were followed and expanded under selection media with puromycin (2μg/ml) and storage for further characterization (data not shown).

References

1. Maxfield FR, Tabas I. Role of cholesterol and lipid organization in disease. *Nature*. 2005;438:612–621.

2. Ikonen E. Mechanisms for Cellular Cholesterol Transport : Defects and Human Disease. *Physiol Rev*. 2006;84:1237–1261.

3. Song Y, et al. Cholesterol-induced toxicity: An integrated view of the role of cholesterol in multiple diseases. *Cell Metab*. 2021;33(10):1911–1925.

4. Brown MS, Goldstein JL. A receptor-mediated pathway for cholesterol homeostasis. *Science (1979)*. 1986;232(4746):34–47.

5. Goldstein JL, et al. Role of lysosomal acid lipase in the metabolism of plasma low density lipoprotein. Observations in cultured fibroblasts from a patient with cholesteryl ester storage disease. *Journal of Biological Chemistry*. 1975;250(21):8487–8495.

6. Infante RE, et al. NPC2 facilitates bidirectional transfer of cholesterol between NPC1 and lipid bilayers, a step in cholesterol egress from lysosomes. *PNAS*. 2008;105(40):15287–15292.

7. Ikonen E. Cellular cholesterol trafficking and compartmentalization. *Nat Rev Mol Cell Biol*. 2008;9:125–138.

8. Heybrock S, et al. Lysosomal integral membrane protein-2 (LIMP-2/SCARB2) is involved in lysosomal cholesterol export. *Nat Commun*. 2019;10:3521.

9. Lange Y. Disposition of intracellular cholesterol in human fibroblasts. *Journal Lipid Research*. 1991;32(2):329–339.

10. Brown MS, Goldstein JL. The SREBP Pathway: Regulation of Cholesterol Metabolism by Proteolysis of a Membrane-Bound Transcription Factor. *Cell*. 1997;89:331–340.

11. Pericleous M, et al. Wolman's disease and cholesteryl ester storage disorder: the phenotypic spectrum of lysosomal acid lipase deficiency. *Lancet Infect Dis*. 2017;2(9):670–679.

12. Vanier MT. Niemann-Pick disease type C. *Orphanet J Rare Dis*. 2010;5:1–18.

13. Reiner Z, et al. Lysosomal acid lipase deficiency - An under-recognized cause of dyslipidaemia and liver dysfunction. *Atherosclerosis*. 2014;235:21–30.

14. Kelly DA, et al. Niemann-Pick disease type C: Diagnosis and outcome in children, with particular reference to liver disease. *J Pediatr*. 1993;123(2):242–247.

15. Haft CR, et al. Human Orthologs of Yeast Vacuolar Protein Sorting Proteins Vps26, 29, and 35: Assembly into Multimeric Complexes. *Mol Biol Cell*. 2000;11:4105–4116.

16. Burd C, Cullen PJ. Retromer: A Master Conductor of Endosome Sorting. *Cold Spring Harb Perspect Biol*. 2014;6:a016774.

17. Wang J, et al. Endosomal receptor trafficking: Retromer and beyond. *Traffic*. 2018;19:578–590.

18. Seaman MNJ. The Retromer Complex : From Genesis to Revelations. *Trends Biochem Sci*. 2021;46(7):608–620.

19. Marquer C, et al. Arf6 controls retromer traffic and intracellular cholesterol distribution via a phosphoinositide-based mechanism. *Nat Commun*. 2016;7:11919.

20. Arighi CN, et al. Role of the mammalian retromer in sorting of the cation-independent mannose 6-phosphate receptor. *J Cell Biol*. 2004;165(1):123–133.

21. Seaman MNJ. Cargo-selective endosomal sorting for retrieval to the Golgi requires retromer. *J Cell Biol*. 2004;165(1):111–122.

22. Dominko K, et al. Impaired Retromer Function in Niemann-Pick Type C Disease Is Dependent on Intracellular Cholesterol Accumulation. *Int J Mol Sci*. 2021;22:13256.

23. Seaman MNJ, Gautreau A, Billadeau DD. Retromer-mediated endosomal protein sorting: all WASHed up! *Trends Cell Biol*. 2013;23(11):522–528.

24. Bartuzi P, et al. CCC- and WASH-mediated endosomal sorting of LDLR is required for normal clearance of circulating LDL. *Nat Commun*. 2016;7(10961):1–11.

25. Fedoseienko A, et al. COMMD Family Regulates Plasma LDL Levels and Attenuates Atherosclerosis Through Stabilizing the CCC Complex in Endosomal LDLR Trafficking. *Circ Res*. 2018;122:1648–1660.

26. Wijers M, et al. The hepatic WASH complex is required for efficient plasma LDL and HDL cholesterol clearance. *JCI Insight*. 2019;4:e126462.

27. de Groot REA, et al. Retromer Dependent Recycling of the Wnt Secretion Factor Wls Is Dispensable for Stem Cell Maintenance in the Mammalian Intestinal Epithelium. *PLoS One*. 2013;8(10):1–9.

28. Ronda OAHO, et al. Measurement of Intestinal and Peripheral Cholesterol Fluxes by a Dual-Tracer Balance Method. *Curr Protoc Mouse Biol*. 2016;6(4):408–434.

29. Neese RA, et al. Measurement of endogenous synthesis of plasma cholesterol in rats and humans using MIDA. *American Journal of Physiology*. 1993;264:E136–E147.

30. van der Veen JN, et al. Activation of the liver X receptor stimulates trans-intestinal excretion of plasma cholesterol. *Journal of Biological Chemistry*. 2009;284(29):19211–19219.

31. de Boer P, et al. Large-scale electron microscopy database for human type 1 diabetes. *Nat Commun*. 2020;(11):2475.

32. Kuipers J, Giepmans BNG. Neodymium as an alternative contrast for uranium in electron microscopy. *Histochem Cell Biol*. 2020;153:271–277.

33. Bligh EG, Dyer WJ. A rapid method of total lipid extraction and purification. *Can J Biochem Physiol*. 1959;37:911–917.

34. Evangelakos I, et al. Oxysterol 7-α hydroxylase (CYP7B1) attenuates metabolic-associated fatty liver disease in mice at thermoneutrality. *Cells*. 2021;10:2656.

35. Vos DY, et al. Cargo-Specific Role for Retriever Subunit VPS26C in Hepatocyte Lipoprotein Receptor Recycling to Control Postprandial Triglyceride-Rich Lipoproteins. *Arterioscler Thromb Vasc Biol*. 2023;43(1):E29–E45.

36. Loregger A, et al. Haploid genetic screens identify SPRING/C12ORF49 as a determinant of SREBP signaling and cholesterol metabolism. *Nat Commun*. 2020;11:1128.

37. Kaizuka T, et al. An Autophagic Flux Probe that Releases an Internal Control. *Mol Cell*. 2016;64(4):835–849.

38. Moffat J, et al. A Lentiviral RNAi Library for Human and Mouse Genes Applied to an Arrayed Viral High-Content Screen. *Cell*. 2006;124:1283–1298.

39. Fischer AW, et al. The adaptor protein PID1 regulates receptor-dependent endocytosis of postprandial triglyceride-rich lipoproteins. *Mol Metab*. 2018;16:88–99.

40. Lin C, et al. Targeting Ligand Independent Tropism of siRNA-LNP by Small Molecules for Directed Therapy of Liver or Myeloid Immune Cells. [published online ahead of print: 2023]; https://doi.org/10.1002/adhm.202202670

41. Müller T, et al. Automated sample preparation with SP3 for low-input clinical proteomics. *Mol Syst Biol*. 2020;16(1):e9111.

42. Cui Y, et al. Retromer has a selective function in cargo sorting via endosome transport carriers. *Journal of Cell Biology*. 2019;218(2):615–631.

43. Carosi JM, et al. Retromer regulates the lysosomal clearance of MAPT/tau. *Autophagy*. 2021;17(9):2217–2237.

44. McNally KE, et al. Retriever is a multiprotein complex for retromer-independent endosomal cargo recycling. *Nat Cell Biol*. 2017;19:1214–1225.

45. Brown MS, Kovanen PT, Goldstein JL. Regulation of plasma cholesterol by lipoprotein receptors. *Science*. 1981;212(4495):628–635.

46. Vos DY, Van De Sluis B. Function of the endolysosomal network in cholesterol homeostasis and metabolic- associated fatty liver disease (MAFLD). *Mol Metab*. 2021;50:101146.

47. Zavodszky E, et al. Mutation in VPS35 associated with Parkinson's disease impairs WASH complex association and inhibits autophagy. *Nat Commun*. 2014;5(May):1–16.

48. Maruzs T, et al. Retromer Ensures the Degradation of Autophagic Cargo by Maintaining Lysosome Function in Drosophila. *Traffic*. 2015;16(10):1088–1107.

49. Daly JL, et al. Multiomic Approach Characterises the Neuroprotective Role of Retromer in Regulating Lysosomal Health. *Nat Commun*. 2023;14:3086.

50. Komatsu M, et al. Impairment of starvation-induced and constitutive autophagy in Atg7-deficient mice. *J Cell Biol*. 2005;169(3):425–434.

51. Liscum L, Faust JR. Low density lipoprotein (LDL)-mediated suppression of cholesterol synthesis and LDL uptake is defective in Niemann-Pick type C fibroblasts. *Journal of Biological Chemistry*. 1987;262(35):17002–17008.

52. Liu B, et al. Reversal of defective lysosomal transport in NPC disease ameliorates liver dysfunction and neurodegeneration in the npc1-/- mouse. *Proc Natl Acad Sci U S A*. 2009;106(7):2377–2382.

53. Aqul A, et al. Hepatic entrapment of esterified cholesterol drives continual expansion of whole body sterol pool in lysosomal acid lipase-deficient mice. *Am J Physiol Gastrointest Liver Physiol*. 2014;307(8):G836–G847.

54. Dietschy JM, Turley SD, Spady DK. Role of liver in the maintenance of cholesterol and low density lipoprotein homeostasis in different animal species, including humans. *J Lipid Res*. 1993;34:1637–1659.

55. Arnaboldi L, et al. LIPA gene mutations affect the composition of lipoproteins: Enrichment in ACAT-derived cholesteryl esters. *Atherosclerosis*. 2020;297(January):8–15.

56. Parini P, et al. ACAT2 Is Localized to Hepatocytes and Is the Major Cholesterol-Esterifying Enzyme in Human Liver. *Circulation*. 2004;110(14):2017–2023.

57. Lee RG, et al. ACAT2 contributes cholesteryl esters to newly secreted VLDL , whereas LCAT adds cholesteryl ester to LDL in mice. *Journal Lipid Research*. 2005;46(6):1205–1212.

58. Steinberg F, et al. A global analysis of SNX27-retromer assembly and cargo specificity reveals a function in glucose and metal ion transport. *Nat Cell Biol*. 2013;15(5):461–471.

59. Gelsthorpe ME, et al. Niemann-Pick type C1 I1061T mutant encodes a functional protein that is selected for endoplasmic reticulum-associated degradation due to protein misfolding. *Journal of Biological Chemistry*. 2008;283(13):8229–8236.

60. Schultz ML, et al. Coordinate regulation of mutant NPC1 degradation by selective ER autophagy and MARCH6-dependent ERAD. *Nat Commun*. 2018;9(1). https://doi.org/10.1038/s41467-018-06115-2

61. Vonk WIM, et al. The copper-transporting capacity of ATP7A mutants associated with Menkes disease is ameliorated by COMMD1 as a result of improved protein expression. *Cell Mol Life Sci*. 2012;69:149–163.

62. Small SA, et al. Model-guided microarray implicates the retromer complex in Alzheimer's disease. *Ann Neurol*. 2005;58(6):909–919.

63. Vilariño-Güell C, et al. VPS35 Mutations in Parkinson Disease. *Am J Hum Genet*. 2011;89(1):162–167.

64. Zimprich A, et al. A mutation in VPS35, encoding a subunit of the retromer complex, causes late-onset Parkinson Disease. *Am J Hum Genet*. 2011;89(1):168–175.

65. Markmann S, et al. Quantitative proteome analysis of mouse liver lysosomes provides evidence for mannose 6-phosphate-independent targeting mechanisms of acid hydrolases in mucolipidosis II. *Molecular and Cellular Proteomics*. 2017;16(3):438–450.

66. Ghosh P, Dahms NM, Kornfeld S. Mannose 6-phosphate receptors: New twists in the tale. *Nat Rev Mol Cell Biol*. 2003;4(3):202–212.

67. Follett J, et al. The Vps35 D620N Mutation Linked to Parkinson's Disease Disrupts the Cargo Sorting Function of Retromer. *Traffic*. 2014;15(2):230–244.

68. Bugarcic A, et al. Vps26A and Vps26B Subunits Define Distinct Retromer Complexes. *Traffic*. 2011;12(12):1759–1773.

69. Rojas R, et al. Regulation of retromer recruitment to endosomes by sequential action of Rab5 and Rab7. *Journal of Cell Biology*. 2008;183(3):513–526.

70. Buratta S, et al. Lysosomal Exocytosis, Exosome Release and Secretory Autophagy: The Autophagic- and Endo-Lysosomal Systems Go Extracellular. *Int J Mol Sci*. 2020;21:2576.

71. Strauss K, et al. Exosome Secretion Ameliorates Lysosomal Storage of Cholesterol in Niemann-Pick Type C Disease. *Journal of Biological Chemistry*. 2010;285(34):26279–26288.

72. Samie MA, Xu H. Lysosomal exocytosis and lipid storage disorders. *J Lipid Res*. 2014;55:995–1009.

73. Peng X, et al. IKKβ activation promotes amphisome formation and extracellular vesicle secretion in tumor cells. *BBA - Molecular Cell Research*. 2021;1868:118857.

74. Eitan E, et al. Impact of lysosome status on extracellular vesicle content and release. *Ageing Res Rev*. 2016;32:65–74.

75. Alvarez-Erviti L, et al. Neurobiology of Disease Lysosomal dysfunction increases exosome-mediated alpha-synuclein release and transmission. *Neurobiol Dis*. 2011;42(3):360–367.

76. Vingtdeux V, et al. Alkalizing Drugs Induce Accumulation of Amyloid Precursor Protein By-products in Luminal Vesicles of Multivesicular Bodies * □. *Journal of Biological Chemistry*. 2007;282(25):18197–18205.

77. Leidal AM, et al. The LC3-Conjugation Machinery Specifies the Loading of RNA- Binding Proteins into Extracellular Vesicles. *Nat Cell Biol*. 2020;22(2):187–199.

78. Minakaki G, et al. Autophagy inhibition promotes SNCA / alpha- synuclein release and transfer via extracellular vesicles with a hybrid autophagosome-exosome- like phenotype. *Autophagy*. 2018;14(1):98–119.

79. Greening DW, et al. Secreted primary human malignant mesothelioma exosome signature reflects oncogenic cargo. *Sci Rep*. 2016;6:32643.

80. Tanida I, Ueno T, Kominami E. LC3 and Autophagy. *Methods Mol Biol*. 2008;445:77–88.

81. Millat G, et al. Niemann-Pick C1 disease: Correlations between NPC1 mutations, levels of NPC1 protein, and phenotypes emphasize the functional significance of the putative sterol-sensing domain and of the cysteine-rich luminal loop. *Am J Hum Genet*. 2001;68(6):1373–1385.

82. Blom TS, et al. Defective endocytic trafficking of NPC1 and NPC2 underlying infantile Niemann-Pick type C disease. *Hum Mol Genet*. 2003;12(3):257–272.

83. Tängemo C, et al. Niemann-Pick type C disease: Characterizing lipid levels in patients with variant lysosomal cholesterol storage. *J Lipid Res*. 2011;52(4):813–825.

84. Brown MS, Goldstein JL. Receptor-mediated control of cholesterol metabolism. *Science (1979)*. 1976;191:150–154.

85. Rohlmann A, et al. Inducible Inactivation of Hepatic LRP Gene by Cre-mediated Recombination Confirms Role of LRP in Clearance of Chylomicron Remnants. *J Clin Invest*. 1998;101:689–695.

86. Phillips-Krawczak CA, et al. COMMD1 is linked to the WASH complex and regulates endosomal trafficking of the copper transporter ATP7A. *Mol Biol Cell*. 2015;26(1):91–103.

87. McNally KE, Cullen PJ. Endosomal Retrieval of Cargo: Retromer Is Not Alone. *Trends Cell Biol*. 2018;28(10):807–822.

88. Gordts PLSM, et al. Impaired LDL Receptor-Related Protein 1 Translocation Correlates with Improved Dyslipidemia and Atherosclerosis in apoE-Deficient Mice. *PLoS One*. 2012;7:1–12.

89. Jaeschke A, et al. Mutation in the distal NPxY motif of LRP1 alleviates dietary cholesterol-induced dyslipidemia and tissue inflammation. *J Lipid Res*. 2021;62:100012.

90. Rovelet-Lecrux A, et al. De novo deleterious genetic variations target a biological network centered on Aβ peptide in early-onset Alzheimer disease. *Mol Psychiatry*. 2015;20(9):1046–1056.

91. Wen L, et al. VPS35 haploinsufficiency increases Alzheimer's disease neuropathology. *Journal of Cell Biology*. 2011;195(5):765–779.

92. Simoes S, et al. Tau and other proteins found in Alzheimer's disease spinal fluid are linked to retromer-mediated endosomal traffic in mice and humans. *Sci Transl Med*. 2020;12(571). https://doi.org/10.1126/scitranslmed.aba6334

93. Liu JP, et al. Cholesterol involvement in the pathogenesis of neurodegenerative diseases. *Molecular and Cellular Neuroscience*. 2010;43(1):33–42.

94. Dai L, et al. Cholesterol Metabolism in Neurodegenerative Diseases: Molecular Mechanisms and Therapeutic Targets. *Mol Neurobiol*. 2021;58(5):2183–2201.

95. Feringa FM, van der Kant R. Cholesterol and Alzheimer's Disease; From Risk Genes to Pathological Effects. *Front Aging Neurosci*. 2021;13(June):1–17.

96. Leopold C, et al. Hepatocyte-specific lysosomal acid lipase deficiency protects mice from diet-induced obesity but promotes hepatic inflammation. *Biochim Biophys Acta Mol Cell Biol Lipids*. 2019;1864(4):500–511.

97. Liu D, et al. Squalene epoxidase drives NAFLD-induced hepatocellular carcinoma and is a pharmaceutical target. *Sci Transl Med*. 2018;10(437). https://doi.org/10.1126/scitranslmed.aap9840

98. Zhou F, Sun X. Cholesterol Metabolism: A Double-Edged Sword in Hepatocellular Carcinoma. *Front Cell Dev Biol*. 2021;9(November):1–10.

99. Huang B, Song BL, Xu C. Cholesterol metabolism in cancer: mechanisms and therapeutic opportunities. *Nat Metab*. 2020;2(2):132–141.

100. Zhang G, et al. DNA and RNA sequencing identified a novel oncogene VPS35 in liver hepatocellular carcinoma. *Oncogene*. 2020;39:3229–3244.

Figure 1

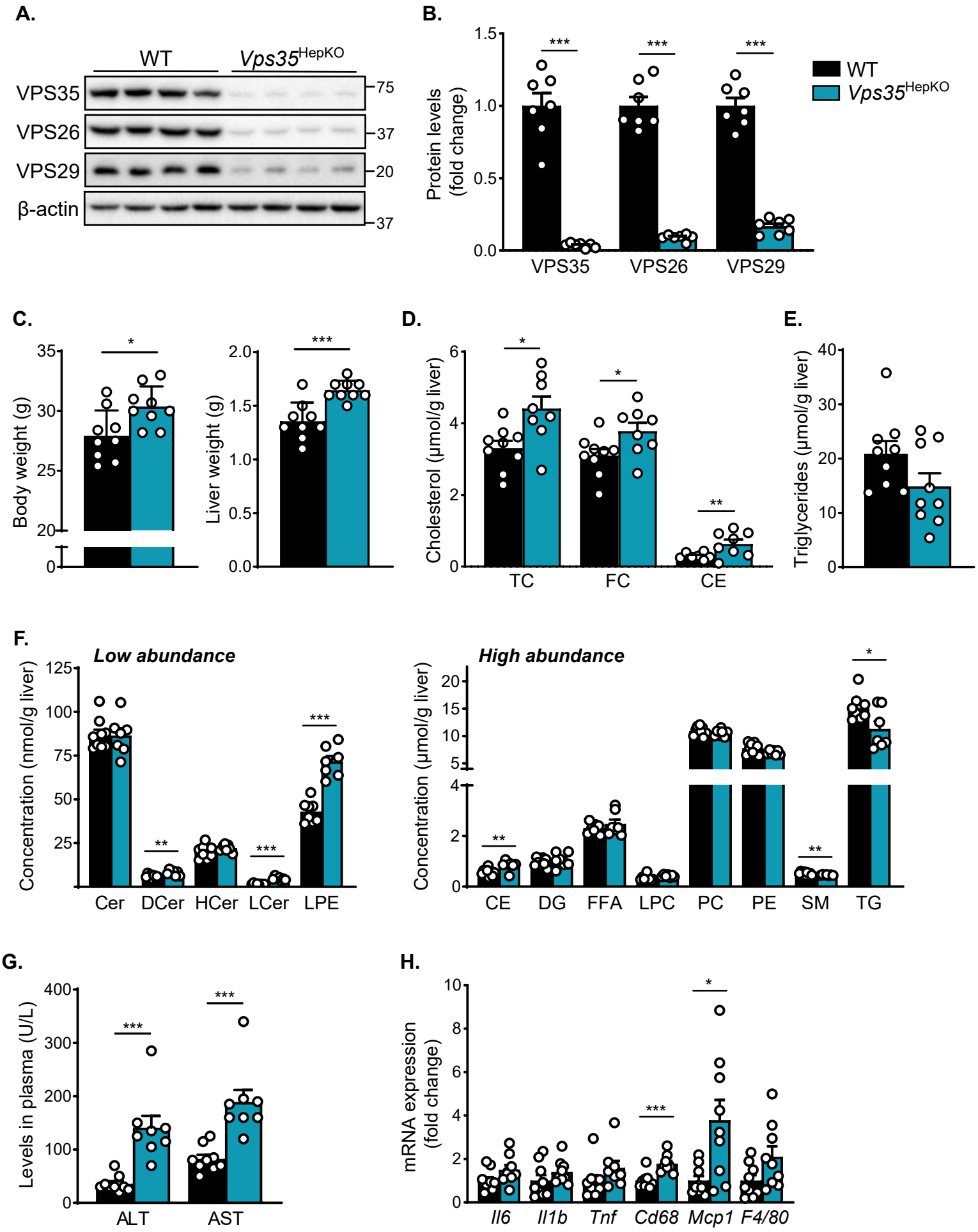
A.
WT
Vps35HepKO
VPS35
VPS26
VPS29
β-actin
75
37
20
37
B.
Protein levels (fold change)
1.5
1.0
0.5
0.0
***
WT
Vps35HepKO
VPS35
VPS26
VPS29
C.
Body weight (g)
35
30
25
20
0
*
Liver weight (g)
2.0
1.5
1.0
0.5
0.0
***
D.
Cholesterol (µmol/g liver)
6
4
2
0
*
**
TC
FC
CE
E.
Triglycerides (µmol/g liver)
40
30
20
10
0
F.
Low abundance
Concentration (nmol/g liver)
125
100
75
50
25
**
***
Cer
DCer
HCer
LCer
LPE
High abundance
Concentration (µmol/g liver)
20
15
10
5
4
2
0
**
*
CE
DG
FFA
LPC
PC
PE
SM
TG
G.
Levels in plasma (U/L)
400
300
200
100
0
***
ALT
AST
H.
mRNA expression (fold change)
10
8
6
4
2
0
*
***
Il6
Il1b
Tnf
Cd68
Mcp1
F4/80

Figure 2

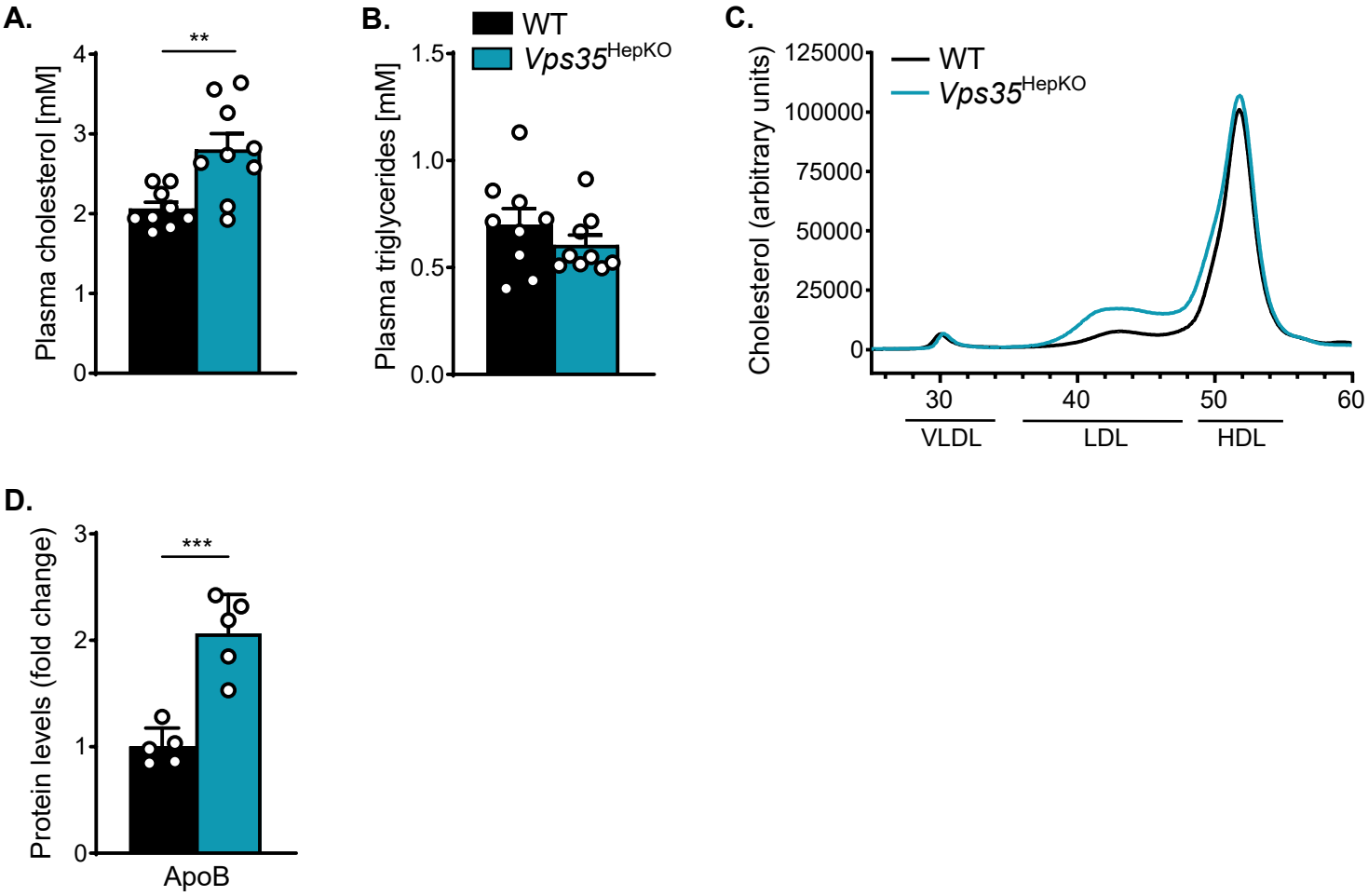
A.
**
Plasma cholesterol [mM]
0
1
2
3
4
B.
WT
Vps35HepKO
Plasma triglycerides [mM]
0.0
0.5
1.0
1.5
C.
WT
Vps35HepKO
Cholesterol (arbitrary units)
0
25000
50000
75000
100000
125000
30
40
50
60
VLDL
LDL
HDL
D.
***
Protein levels (fold change)
0
1
2
3
ApoB

Figure 3

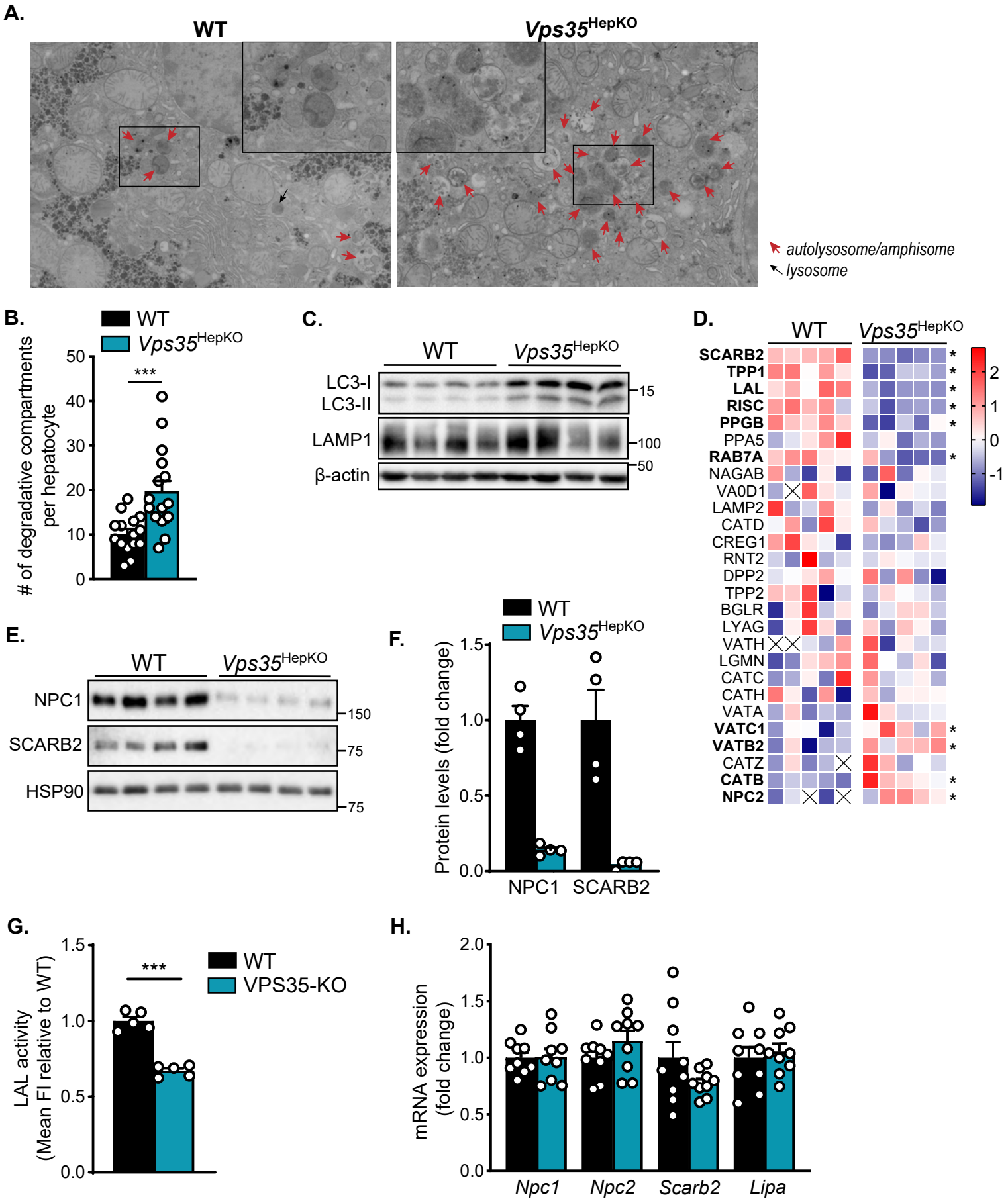
A.
WT
Vps35HepKO
autolysosome/amphisome
lysosome
B.
WT
Vps35HepKO
# of degradative compartments per hepatocyte
***
C.
WT
Vps35HepKO
LC3-I
LC3-II
LAMP1
β-actin
15
100
50
D.
WT
Vps35HepKO
SCARB2
TPP1
LAL
RISC
PPGB
PPA5
RAB7A
NAGAB
VA0D1
LAMP2
CATD
CREG1
RNT2
DPP2
TPP2
BGLR
LYAG
VATH
LGMN
CATC
CATH
VATA
VATC1
VATB2
CATZ
CATB
NPC2
E.
WT
Vps35HepKO
NPC1
SCARB2
HSP90
150
75
75
F.
WT
Vps35HepKO
Protein levels (fold change)
NPC1
SCARB2
G.
WT
VPS35-KO
LAL activity (Mean FI relative to WT)
***
H.
mRNA expression (fold change)
Npc1
Npc2
Scarb2
Lipa

Figure 4

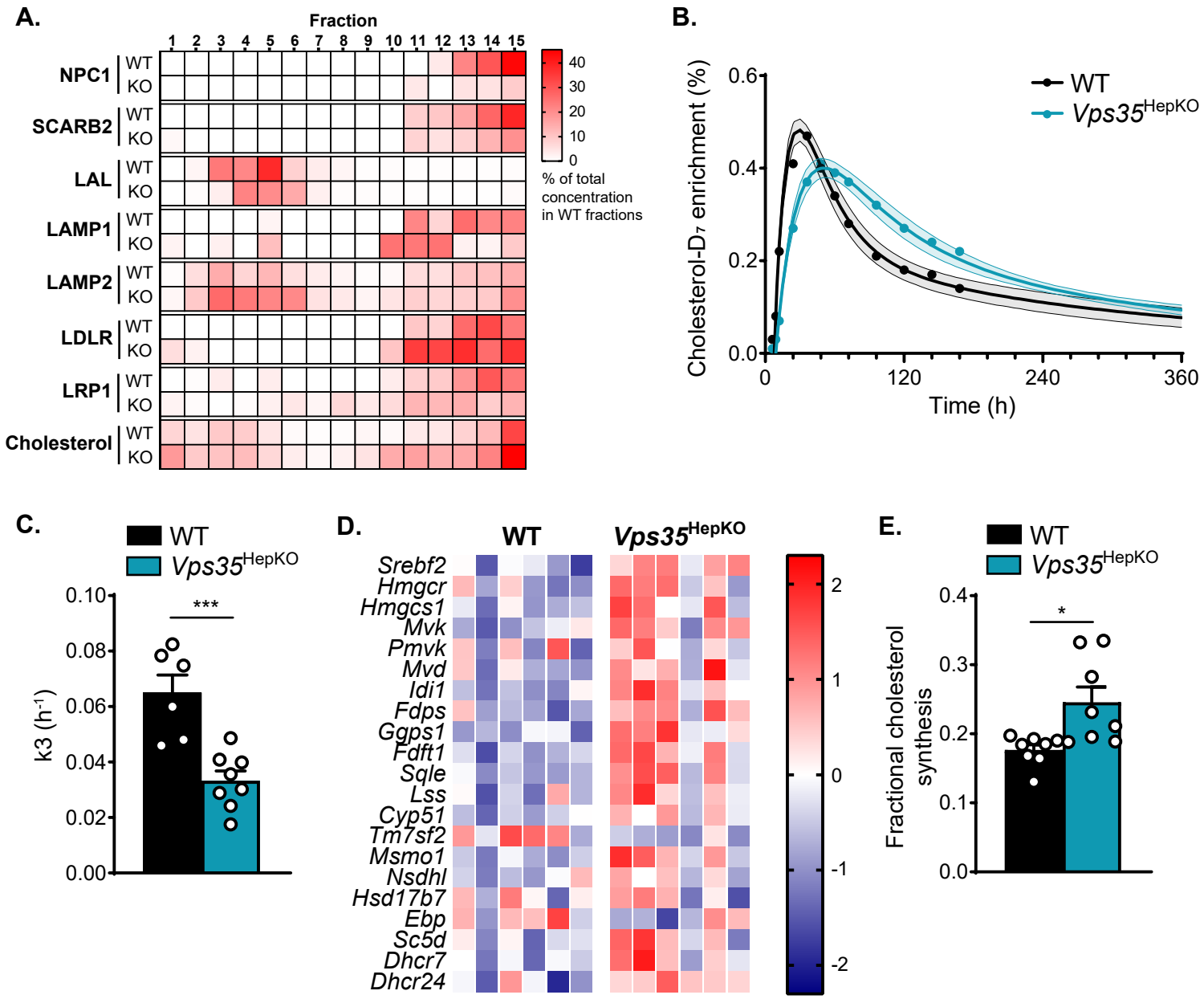
A.
Fraction
1 2 3 4 5 6 7 8 9 10 11 12 13 14 15
NPC1
SCARB2
LAL
LAMP1
LAMP2
LDLR
LRP1
Cholesterol
WT
KO
40
30
20
10
0
% of total concentration in WT fractions
B.
Cholesterol-D7 enrichment (%)
0.6
0.4
0.2
0.0
0
120
240
360
Time (h)
WT
Vps35HepKO
C.
WT
Vps35HepKO
k3 (h-1)
0.10
0.08
0.06
0.04
0.02
0.00
***
D.
WT
Vps35HepKO
Srebf2
Hmgcr
Hmgcs1
Mvk
Pmvk
Mvd
Idi1
Fdps
Ggps1
Fdft1
Sqle
Lss
Cyp51
Tm7sf2
Msmo1
Nsdhl
Hsd17b7
Ebp
Sc5d
Dhcr7
Dhcr24
2
1
0
-1
-2
E.
WT
Vps35HepKO
Fractional cholesterol synthesis
0.4
0.3
0.2
0.1
0.0
*

Figure 5

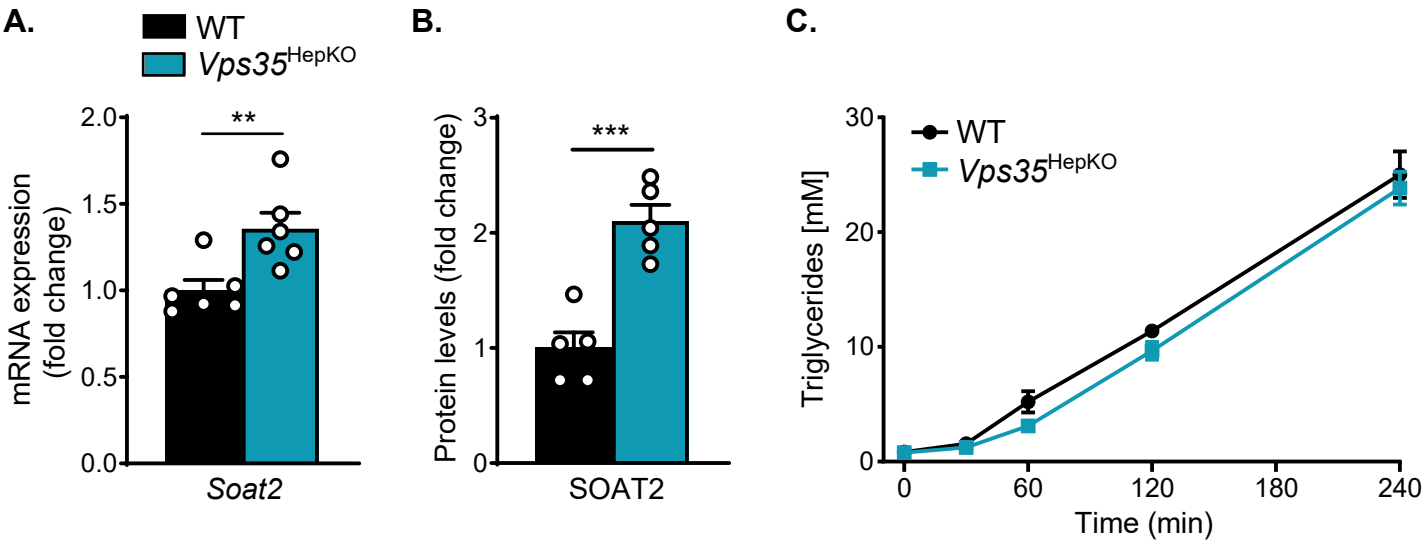

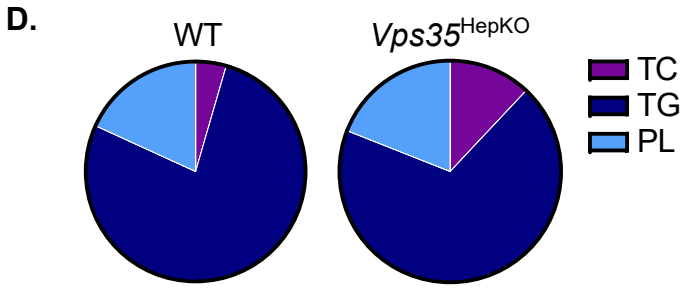

	WT	*Vps35*^{HepKO}
TC (%)	4.5 ± 0.5	12.0 ± 1.4#
TG (%)	77.2 ± 0.8	69.0 ± 2.8*
PL (%)	18.3 ± 1.1	19.0 ± 1.8
ApoB48 (%)	85.2 ± 0.9	84.1 ± 0.5
ApoB100 (%)	14.8 ± 0.9	15.9 ± 0.5

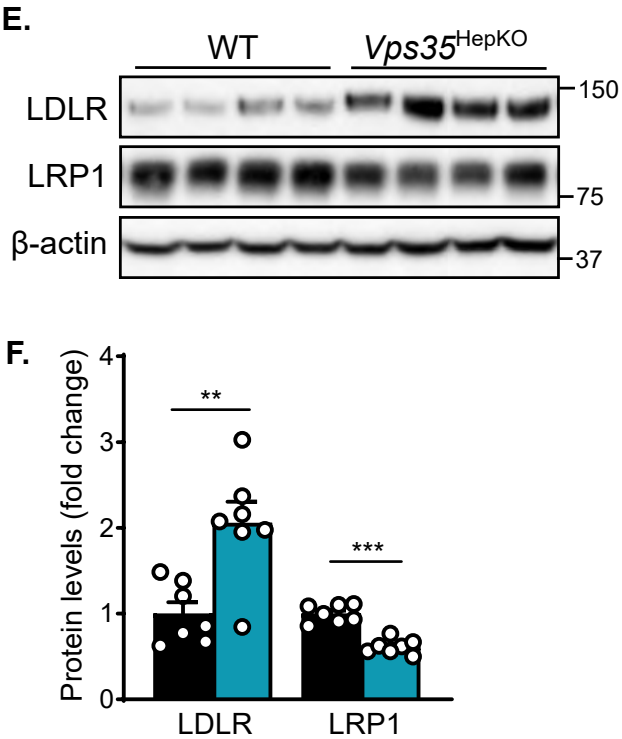

Figure 6

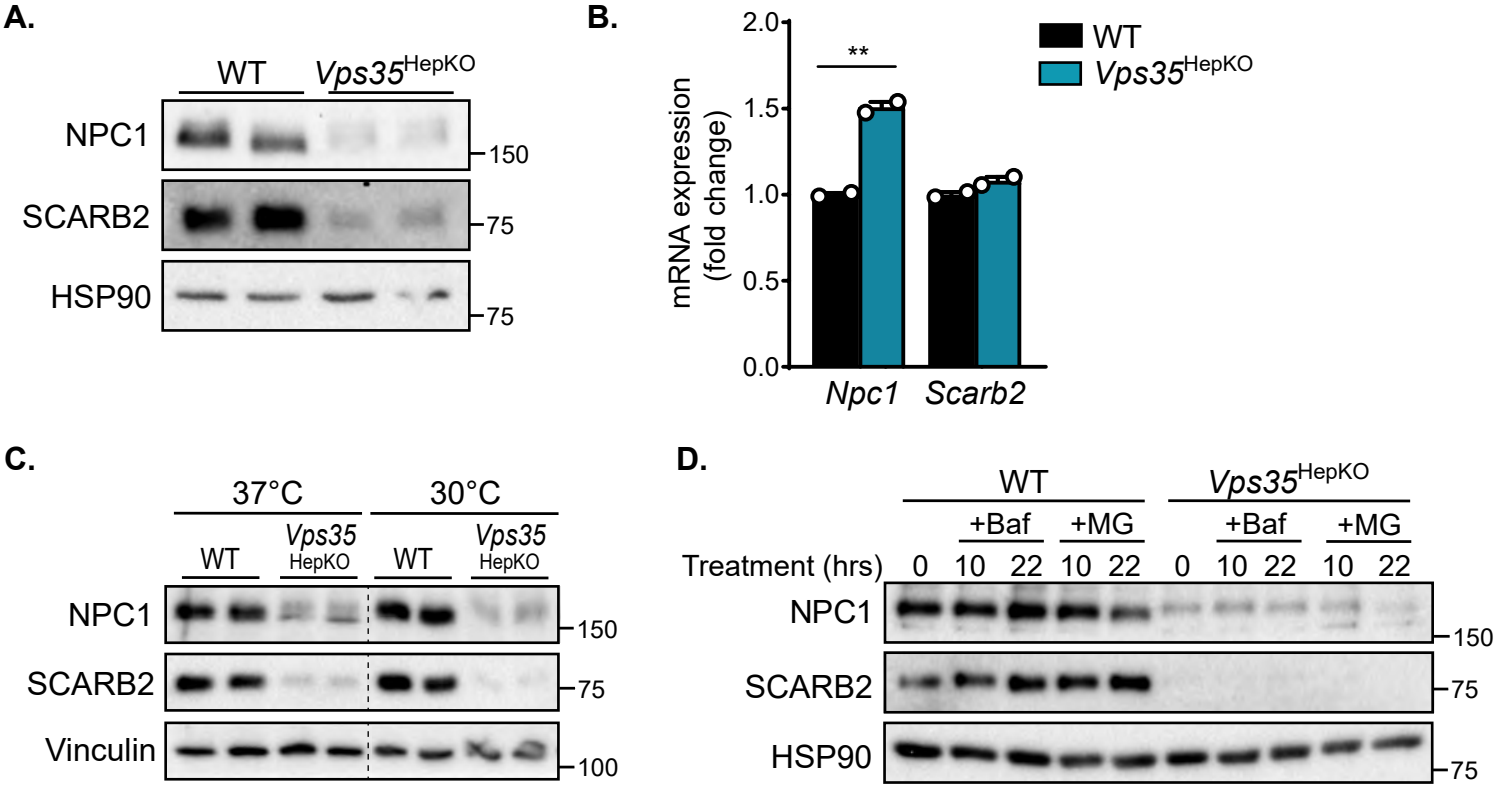
A.
WT
Vps35HepKO
NPC1
SCARB2
HSP90
150
75
75
B.
WT
Vps35HepKO
**
mRNA expression (fold change)
2.0
1.5
1.0
0.5
0.0
Npc1
Scarb2
C.
37°C
30°C
WT
Vps35 HepKO
WT
Vps35 HepKO
NPC1
SCARB2
Vinculin
150
75
100
D.
WT
Vps35HepKO
+Baf
+MG
+Baf
+MG
Treatment (hrs)
0 10 22 10 22 0 10 22 10 22
NPC1
SCARB2
HSP90
150
75
75

Figure 7

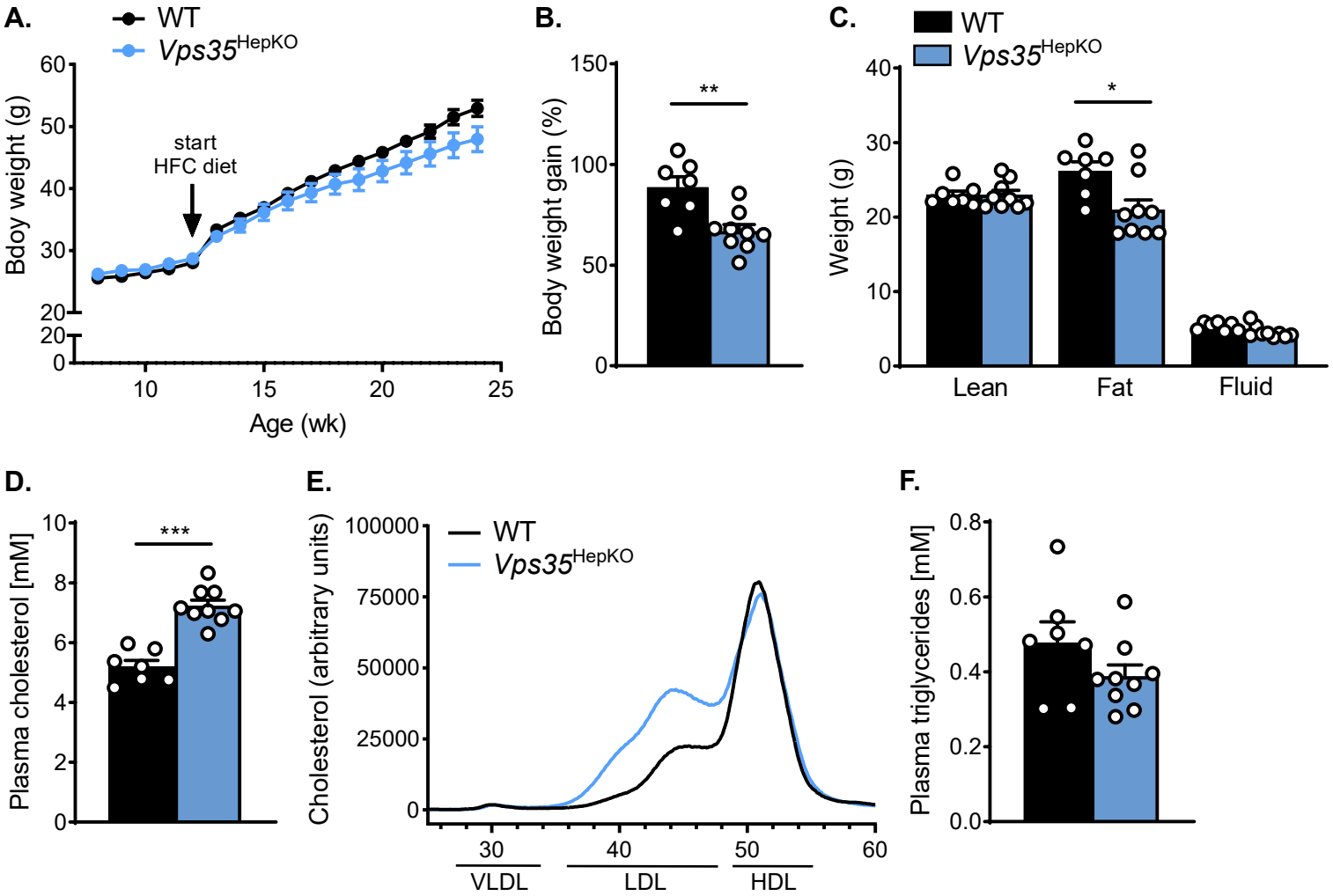
A.
WT
Vps35HepKO
Bdoy weight (g)
start
HFC diet
Age (wk)
B.
Body weight gain (%)
**
C.
WT
Vps35HepKO
Weight (g)
*
Lean
Fat
Fluid
D.
Plasma cholesterol [mM]
***
E.
Cholesterol (arbitrary units)
WT
Vps35HepKO
VLDL
LDL
HDL
F.
Plasma triglycerides [mM]

Figure 8

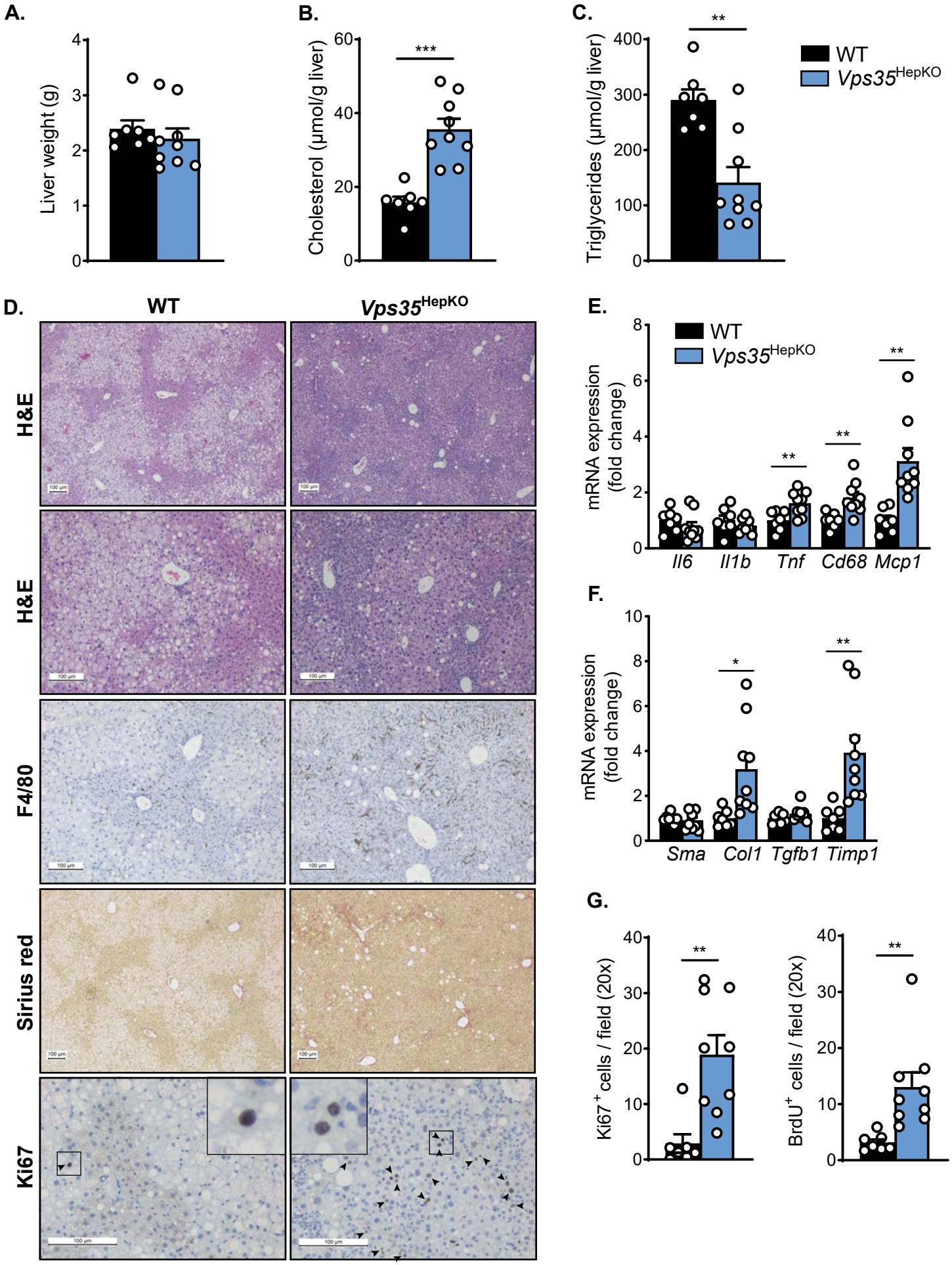
A.
Liver weight (g)
0
1
2
3
4
B.
Cholesterol (µmol/g liver)
0
20
40
60
***
C.
Triglycerides (µmol/g liver)
0
100
200
300
400
**
WT
Vps35HepKO
D.
WT
Vps35HepKO
H&E
H&E
F4/80
Sirius red
Ki67
E.
mRNA expression (fold change)
0
2
4
6
8
WT
Vps35HepKO
**
**
**
Il6
Il1b
Tnf
Cd68
Mcp1
F.
mRNA expression (fold change)
0
2
4
6
8
10
*
**
Sma
Col1
Tgfb1
Timp1
G.
Ki67+ cells / field (20x)
0
10
20
30
40
**
BrdU+ cells / field (20x)
0
10
20
30
40
**